

Observed properties of FRII quasars and radio galaxies at $z < 1.0$

L. M. Mullin^{1*}, J. M. Riley^{1†} and M. J. Hardcastle^{2‡}

¹*Astrophysics Group, Cavendish Laboratory, University of Cambridge, J J Thomson Avenue, Cambridge CB3 0HE*

²*School of Physics, Astronomy and Mathematics, University of Hertfordshire, College Lane, Hatfield AL10 9AB*

ABSTRACT

In a long-term observing project we have imaged a complete sample of FRII quasars and radio galaxies with $z < 1.0$ at high resolution and high sensitivity with the VLA and MERLIN. This sample of 98 sources includes 15 quasars, 11 broad line radio galaxies and 57 narrow line radio galaxies, allowing unification to be considered in terms of source morphological properties. Radio maps of all the targets have been presented in earlier papers. Here we carry out a systematic analysis of the properties of the jets, cores, lobes and hotspots of objects in the sample. The majority of the tests that we perform show that the data are consistent with a model in which quasars and broad-line radio galaxies are unified with narrow-line objects. Relativistic beaming is the main effect that determines the properties of kiloparsec-scale jets, and it may also have some effect on hotspots. However, some properties of the sample are difficult to account for in simple unified models.

Key words: galaxies:active - galaxies:jets - radio continuum: galaxies

1 INTRODUCTION

Fanaroff & Riley (1974) type II radio sources (hereafter FRIIs) are powerful sources associated with bipolar outflows that extend great distances from the central engine, remaining highly collimated as they do so. They can be divided into different classes based on features of their optical spectra: radio-loud quasars (Qs), broad line radio galaxies (BLRGs), narrow line radio galaxies (NLRGs) and low excitation radio galaxies (LERGs) can all be FRIIs. A principal defining characteristic is the presence, or absence, of broad line emission, with the Qs and BLRGs having both broad and narrow line emission lines, the NLRGs having narrow line emission only and the LERGs lacking strong high-excitation lines of either type (Hine & Longair 1979; Laing et al. 1994).

The current standard unification scheme proposes that the Qs, BLRGs and (at least some of) the NLRGs are intrinsically part of the same population (Scheuer 1987; Barthel 1987, 1989). In this model, the broad emission line region lies close to the very compact central engine and is surrounded by a dusty torus, whereas the narrow line emission region lies further out. Sources that are viewed along or close to the axis of the torus show both broad and narrow line emission – these are the Qs and BLRGs, which we refer to collectively as broad-line objects – but the broad line emission region is obscured for those that are oriented closer to the plane of the sky, the NLRGs. Thus differences in the orientation of the source axis to the observer’s line of sight are the origin of the three spectral classes. The LERGs lie outside of this scheme; it has been suggested (e.g. Barthel 1994) that LERGs form part of the

parent population of BL Lac objects rather than core-dominated Qs and should not show broad line emission at any angle to the line-of-sight, a model consistent with their nuclear properties at other wavebands (Chiaberge, Capetti & Celotti 2002; Hardcastle, Evans & Croston 2006).

An important detail of the model arises from the fact that the observed luminosity distributions of Qs and BLRGs are not the same. Qs are more powerful and found at higher redshifts (or, equivalently in a flux-limited sample, higher radio luminosities) than the BLRGs; for example, in the 3CR sample (Bennett 1962) Qs are found only with $z \gtrsim 0.3$, while BLRGs are found with $z \lesssim 0.3$. It has been suggested that BLRGs may be the low-luminosity equivalents of Qs, or that they lie near the critical angle dividing the quasars and radio galaxies (Barthel 1989; Hardcastle et al. 1998, hereafter H98). While some high-luminosity BLRGs may indeed be intermediate objects, it is clear that at low luminosity, where there are no Qs, BLRGs are the only candidate for the aligned counterpart of the population of low-luminosity NLRGs.

Often FRIIs exhibit a bright linear feature called a jet that extends at least some of the distance between the central feature, the core, and the bright hotspot at the end of the lobe. The jets in most FRIIs are one-sided: either no counterjet is seen or it is much fainter than the feature that is identified as the jet. Relativistic beaming of the jet emission is invoked to explain this asymmetry, as the large scale lobe morphology appears otherwise roughly symmetric. The jet detection rate is higher for Qs and BLRGs than for NLRGs; this can be explained in unified models, since for the broad-line objects the beamed jet is aligned closer to the line of sight and appears brighter. The jet detection rate for LERGs is the highest of all classes (e.g. Mullin, Hardcastle & Riley 2006) which may be re-

* E-mail: mullin@extragalactic.info (LMM)

† E-mail: julia@mrao.cam.ac.uk (JMR)

‡ m.j.hardcastle@herts.ac.uk (MJH)

lated to systematic environmental differences between some of the LERGs and the other emission-line types (Hardcastle 2004).

Further evidence in support of relativistic beaming in jets is provided by the Laing-Garrington effect (Laing 1988; Garrington et al. 1988), which is the association of the jet side with the less depolarized lobe. High-resolution multi-frequency observations indicate that the depolarization occurs in an external Faraday screen, so that the less depolarized lobe is expected to be the lobe closer to us; any tendency for the (brighter) jet to be associated with this lobe then implies that beaming is an important factor in jet detection (Scheuer 1987).

While various aspects of the unification and beaming model have been tested and discussed in the literature, there has been little work using complete samples of radio sources free from orientation bias that include sufficient numbers of objects of all spectral classes to give statistically significant results. Good quality observations of such a sample, with both high resolution and sensitivity, are therefore vital, and this has been the rationale behind a long-term observational project in which we have mapped a complete sample of the brightest FR II radio sources with $z < 1.0$. The sample, which is defined in section 2, includes 98 sources. Maps of these have been presented in a series of papers: Black et al. (1992), Leahy et al. (1997), Hardcastle et al. (1997), Gilbert et al. (2004) and Mullin, Hardcastle & Riley (2006). These maps are available online¹ along with a database of all measurements analysed and discussed in this paper. The sample includes 15 Qs, 11 BLRGs and 57 NLRGs, thus enabling aspects of unification to be tested along with trends in source properties over the wide redshift and luminosity range spanned by the data. In section 2 we also define a number of morphological and flux parameters corresponding to the observed source properties and describe our measurement methods.

We examine the properties of the lobes, cores and jets and hotspots in sections 3, 4 and 5 respectively. For each feature, observational effects are considered as well as trends across the power, redshift and source size range of the sample and we quantify these where appropriate with statistical tests. The significance of linear correlation is tested for using Spearman's rank correlation coefficient. For the core and jet prominence data, however, this is not possible as only upper limits on these parameters are available for some sources: in statistical terminology, the data are censored. Instead, a modified Kendall's τ rank correlation coefficient as implemented in the survival-analysis package ASURV (LaValley, Isobe & Feigelson 1992) is used for these data. The Kolmogorov-Smirnov (hereafter K-S) test determines if it is the case that the cumulative distribution function of two samples differ and is used to address the question of whether some property of two subsamples of the data (that is, subsamples defined by power, redshift and size cutoffs or by spectral class) differ significantly. It is sensitive to differences in both location and shape of the functions. No modification of the K-S test to take account of censoring is available to us, and so we do not use it in situations where censoring is important. The Wilcoxon-Mann-Whitney (hereafter W-M-W) test is also used to determine if two defined subsamples differ, but in this case the null hypothesis tested is that the probability of an observation of one population exceeding an observation from the second is 0.5. Thus the W-M-W test is used to determine whether there is a significant difference in the magnitude of the quantity of interest between the two subsamples, that is, if one dataset has significantly smaller or larger values than the other. In order to treat censored data correctly when

testing for such differences, a generalized W-M-W test is used, the Peto-Prentice test, which is implemented in ASURV. Finally, the binomial test is used to determine the statistical significance of any correlation with jet or longer lobe side for a number of properties. The significance of all test results is discussed in the text and the results are tabulated. We take a result to be significant enough to be discussed if the null hypothesis is rejected at better than the 95 per cent confidence level.

The interpretation of the observed properties of our sample sources, and the evidence for and against unified models, is discussed in section 6. The quantitative implications of our results for beaming in the cores and jets of powerful radio galaxies will be discussed in a separate paper.

The spectral index, α , is defined throughout the paper in the sense that $S = \nu^{-\alpha}$ (where S is the flux and ν denotes the frequency) and we assume that $H_0 = 70 \text{ kms}^{-1}\text{Mpc}^{-1}$, $\Omega_m = 0.3$ and $\Omega_\Lambda = 0.7$.

2 THE DATA

2.1 The Sample

The sample is selected from the complete flux-limited sample of Laing, Riley & Longair (1983, hereafter LRL), which is itself based on the 3CR survey. The LRL sample includes all the sources with total source flux densities measured at 178 MHz $S_{178} > 10.9 \text{ Jy}$ (on the scale of Baars et al. 1977) with $\text{dec} > 10^\circ$ and $|b| > 10^\circ$. At this low frequency the source flux is dominated by the emission from the large-scale lobe structure, so that little contribution should be made by Doppler-boosted components, which should ensure the sample is as free as possible from orientation bias. There are 173 LRL sources in total, including 29 FRI and 125 FR II objects. All 98 FR II radio galaxies and quasars with $z < 1.0$ are listed in Table 1, which includes references to all the radio maps from which the data analysed in this paper have been obtained.

2.2 Parameter definitions and measurement methods

2.2.1 Lobe size

Since many sources show distortion and bending in the jet and lobe features, there is no obvious single definition of source size. Shocks associated with the deceleration of the outflow are often assumed to produce the observed hotspot features, in which case the core-hotspot separation should represent a measure of the beam length; however, multiple hotspots are commonly found so the core-hotspot separation as a parametrization of beam length is not without ambiguity. The same ambiguity will affect the lobe size measured along the core-hotspot axis, which could represent the extent of the post-shock flow of beam material along the beam axis. Finally, the largest angular size of the lobe does not always lie along the core-hotspot axis or the apparent flow direction, as a few sources appear distorted with considerable lateral extension in the lobes.

Accordingly, three source length measurements have been made. The angular core-hotspot separation is the angular distance between the core and primary hotspot (defined in section 2.2.6) within a lobe, Θ_{c-hs} , and is measured using the hotspot positions obtained from the highest resolution map available for the source. Θ_l , the angular lobe length, is defined as the maximum angular lobe size measured from the core along the core-primary hotspot axis. The largest angular size of the lobe, Θ_{LAS_1} , is the maximum

¹ See <http://zll.extragalactic.info/>

Table 1. The sample.

Source	IAU Name	RA [h m s]	Dec [$^{\circ}$ ' '']	z	Spectral class	S_{178} [Jy]	α (178–750 MHz)	Maps Freq. [GHz]	Ref.
4C12.03	0007+124	00 07 18.25	+12 27 23.1	0.156	L	10.9	0.87	1.5	1
3C6.1	0013+790	00 13 34.36	+79 00 11.1	0.840	N	13.7	0.68	8.4	2
3C16	0035+130	00 35 09.16	+13 03 39.6	0.405	L	12.2	0.94	8.4	3
3C19	0038+328	00 38 13.80	+32 53 39.7	0.482	N	13.2	0.63	4.5	3
3C20	0040+517	00 40 20.08	+51 47 10.2	0.174	N	46.8	0.66	8.4	4
3C22	0048+509	00 48 04.71	+50 55 45.4	0.937	B	12.1	0.78	8.5	2
3C33	0106+130	01 06 14.54	+13 04 14.8	0.060	N	59.3	0.76	1.5	1
								4.8	5,6
3C33.1	0106+729	01 06 06.48	+72 55 59.2	0.181	B	14.2	0.62	4.9	7
3C34	0107+315	01 07 32.51	+31 31 23.9	0.690	N	11.9	1.06	4.8	2,8
3C35	0109+492	01 09 04.94	+49 12 40.1	0.068	L	11.4	0.77	0.61	9
3C41	0123+329	01 23 54.74	+32 57 38.3	0.794	N	10.6	0.51	8.5	2
3C42	0125+287	01 25 42.68	+28 47 30.4	0.395	N	13.1	0.73	8.5	3
3C46	0132+376	01 32 34.09	+37 38 47.0	0.437	N	11.1	1.13	8.5	3
3C47	0133+207	01 33 40.43	+20 42 10.2	0.425	Q	28.8	0.98	4.9	3,10
3C55	0154+286	01 54 19.50	+28 37 04.8	0.735	N	21.5	1.04	4.8	2,8
3C61.1	0210+860	02 10 37.10	+86 05 18.5	0.186	N	34.0	0.77	1.5	9
								4.9	7
3C67	0221+276	02 21 18.03	+27 36 37.2	0.310	B	10.9	0.58	4.8	3
								8.4	11
3C79	0307+169	03 07 11.48	+16 54 36.9	0.256	N	33.2	0.92	8.4	4
3C98	0356+102	03 56 10.21	+10 17 31.7	0.031	N	51.4	0.78	8.4	12
3C109	0410+110	04 10 54.87	+11 04 41.4	0.306	B	23.5	0.85	8.3	3
4C14.11	0411+141	04 11 40.94	+14 08 48.3	0.206	L	12.1	0.84	8.4	4
3C123	0433+295	04 33 55.21	+29 34 12.6	0.218	L	206.0	0.70	8.4	4
3C132	0453+227	04 53 42.18	+22 44 43.9	0.214	L	14.9	0.68	8.4	4
3C153	0605+480	06 05 44.44	+48 04 48.8	0.277	N	16.7	0.66	8.4	4
3C171	0651+542	06 51 10.83	+54 12 47.6	0.238	N	21.3	0.87	8.1	4
3C172	0659+253	06 59 03.90	+25 18 12.0	0.519	N	16.5	0.86	8.5	3
3C173.1	0702+749	07 02 47.91	+74 54 16.6	0.292	L	16.8	0.88	8.4	4
3C175	0710+118	07 10 15.38	+11 51 24.0	0.768	Q	17.6	0.98	8.4	2
3C175.1	0711+146	07 11 14.28	+14 41 33.9	0.920	N	11.4	0.91	4.9	2
3C184	0733+705	07 33 59.01	+70 30 01.1	0.990	N	13.2	0.86	4.9	2
3C184.1	0734+805	07 34 25.05	+80 33 24.1	0.119	N	14.2	0.68	8.4	12
DA240	0745+560	07 44 34.96	+55 56 29.0	0.036	L	23.2	0.77	0.61	9
3C192	0802+243	08 02 35.50	+24 18 26.4	0.060	N	23.0	0.79	8.2	12
3C196	0809+483	08 09 59.40	+48 22 07.6	0.871	Q	68.2	0.79	4.9	2
3C200	0824+294	08 24 21.43	+29 28 42.2	0.458	N	12.3	0.84	8.5	3
4C14.27	0832+143	08 32 16.51	+14 22 12.1	0.392	N	11.2	1.15	8.5	3
3C207	0838+133	08 38 01.72	+13 23 05.6	0.684	Q	13.6	0.90	4.9	2
3C215	0903+169	09 03 44.14	+16 58 16.1	0.411	Q	12.4	1.06	4.9	10
3C217	0905+380	09 05 41.42	+38 00 29.9	0.898	N	11.3	0.77	4.9	2
3C216	0906+430	09 06 17.27	+43 05 58.6	0.668	Q	20.2	0.84	8.2	2,13
3C219	0917+458	09 17 50.66	+45 51 43.9	0.174	B	44.9	0.81	4.8	14
3C220.1	0926+793	09 26 31.87	+79 19 45.4	0.610	N	15.8	0.93	8.4	2
3C220.3	0931+836	09 31 10.50	+83 28 55.0	0.685	N	15.7	0.75	4.9	2
3C223	0936+361	09 36 50.87	+36 07 35.0	0.137	N	16.0	0.74	8.4	12
3C225B	0939+139	09 39 32.21	+13 59 33.3	0.582	N	23.2	0.94	4.9	3
3C226	0941+100	09 41 36.16	+10 00 03.8	0.818	N	15.0	0.88	8.5	2
4C73.08	0945+734	09 45 09.90	+73 28 22.2	0.058	N	15.6	0.85	0.61	9
3C228	0947+145	09 47 27.63	+14 34 02.5	0.552	N	23.8	1.00	8.5	3
3C234	0958+290	09 58 57.42	+29 01 37.4	0.185	N	34.2	0.86	8.4	4
3C236	1003+351	10 03 05.37	+35 08 48.1	0.099	L	15.7	0.51	0.61	9
4C74.16	1009+748	10 09 49.81	+74 52 29.5	0.810	N	11.7	0.87	8.5	2
3C244.1	1030+585	10 30 19.75	+58 30 05.2	0.428	N	22.1	0.82	8.4	3
3C247	1056+432	10 56 08.38	+43 17 30.6	0.750	N	10.6	0.61	4.9	2
3C249.1	1100+772	11 00 27.32	+77 15 08.6	0.311	Q	11.7	0.81	4.9	3
3C254	1111+408	11 11 53.30	+40 53 41.6	0.734	Q	19.9	0.96	4.9	2
3C263	1137+660	11 37 09.30	+66 04 27.0	0.656	Q	15.2	0.82	4.9	2,10
3C263.1	1140+223	11 40 49.15	+22 23 34.9	0.824	L	18.2	0.87	8.1	2
3C265	1142+318	11 42 52.39	+31 50 29.1	0.811	N	19.5	0.96	4.8	2,15
3C268.1	1157+732	11 57 48.12	+73 17 30.6	0.950	N	21.4	0.59	8.5	2

Source	IAU Name	RA [h m s]	Dec [$^{\circ}$ ' '']	z	Spectral class	S_{178} [Jy]	α (178 – 750 MHz)	Maps Freq. [GHz]	Ref.
3C268.3	1203+645	12 03 54.28	+64 30 18.6	0.371	B	11.7	0.50	5.0	3
3C274.1	1232+216	12 32 56.74	+21 37 05.8	0.422	N	18.0	0.87	8.5	3
3C275.1	1241+166	12 41 27.58	+16 39 18.0	0.557	Q	19.9	0.96	8.5	3
3C277.2	1251+159	12 51 04.20	+15 58 51.2	0.767	N	12.0	1.02	4.9	2
3C280	1254+476	12 54 41.66	+47 36 32.7	0.996	N	23.7	0.81	4.9	2
3C284	1308+277	13 08 41.33	+27 44 02.6	0.239	N	12.3	0.95	8.1	4
3C285	1319+428	13 19 05.22	+42 50 55.7	0.079	L	12.3	0.95	1.6	9
								4.9	16
3C289	1343+500	13 43 27.38	+50 01 32.0	0.967	N	12.0	0.81	4.9	2
3C292	1349+647	13 49 13.07	+64 44 24.4	0.713	N	10.1	0.80	8.5	2
3C295	1409+524	14 09 33.44	+52 26 13.6	0.461	N	91.0	0.63	8.6	3
3C299	1419+419	14 19 06.29	+41 58 30.2	0.367	N	12.9	0.65	4.5	3
3C300	1420+198	14 20 39.96	+19 49 13.2	0.272	N	19.5	0.78	8.1	4
3C303	1441+522	14 41 24.82	+52 14 18.4	0.141	B	12.2	0.76	1.5	1
3C319	1522+546	15 22 43.90	+54 38 38.4	0.192	L	16.7	0.90	8.4	4
3C321	1529+242	15 29 33.42	+24 14 26.2	0.096	N	14.7	0.60	4.8	17
3C325	1549+628	15 49 13.99	+62 50 20.0	0.860	Q	15.6	0.70	4.9	2
3C326	1549+202	15 49 56.13	+20 14 18.2	0.089	B	22.2	0.88	1.4	9
3C330	1609+660	16 09 13.90	+66 04 22.3	0.549	N	30.3	0.71	8.4	3
3C334	1618+177	16 18 07.33	+17 43 29.6	0.555	Q	11.9	0.86	4.9	10
3C336	1622+238	16 22 32.21	+23 52 02.0	0.927	Q	11.5	0.73	4.9	2,10
3C341	1626+278	16 26 02.42	+27 48 13.9	0.448	N	10.8	0.85	8.5	3
3C337	1627+444	16 27 19.07	+44 25 38.2	0.630	N	11.8	0.63	4.9	2
3C340	1627+234	16 27 29.41	+23 26 42.6	0.760	N	10.1	0.73	4.9	2
3C349	1658+471	16 58 04.44	+47 07 20.3	0.205	N	14.5	0.74	8.4	4
3C351	1704+608	17 04 03.49	+60 48 30.9	0.371	Q	14.9	0.73	8.3	3
3C352	1709+460	17 09 18.00	+46 05 06.0	0.806	N	11.3	0.88	4.7	2
3C381	1832+474	18 32 24.47	+47 24 39.0	0.161	B	18.1	0.81	8.4	4
3C382	1833+326	18 33 11.97	+32 39 18.2	0.058	B	21.7	0.59	8.5	18
3C388	1842+455	18 42 35.44	+45 30 21.7	0.091	L	26.8	0.70	4.9	19
3C390.3	1845+797	18 45 37.57	+79 43 06.5	0.056	B	51.8	0.75	8.4	20
3C401	1939+605	19 39 38.81	+60 34 33.5	0.201	L	22.8	0.71	8.4	4
3C427.1	2104+763	21 04 44.80	+76 21 09.5	0.572	L	29.0	0.97	8.5	3
3C436	2141+279	21 41 57.91	+27 56 30.3	0.215	N	19.4	0.86	8.4	4
3C438	2153+377	21 53 45.51	+37 46 12.8	0.290	L	48.7	0.88	8.4	4
3C441	2203+292	22 03 49.27	+29 14 43.8	0.780	N	12.6	0.83	4.9	2,8
3C452	2243+394	22 43 32.79	+39 25 27.3	0.081	N	59.3	0.78	8.5	18
3C455	2252+129	22 52 34.53	+12 57 33.5	0.543	Q	14.0	0.71	4.9	3
3C457	2309+184	23 09 38.53	+18 29 22.0	0.428	N	14.3	1.01	8.5	3

Notes for Table 1. All data from Laing, Riley & Longair (1983) and subsequent updates.

Column [1]: 3CR catalogue source name.

Column [2]: IAU source name (B1950.0).

Column [3]: Right Ascension [h m s] of the optical ID (B1950.0).

Column [4]: Declination [$^{\circ}$ ' ''] of the optical ID (B1950.0).

Column [5]: Redshift, rounded to 3 decimal places.

Column [6]: Optical type. B: broad emission line radio galaxy, L: low excitation radio galaxy, N: narrow emission line radio galaxy, Q: quasar.

Column [9]: Total flux density for the source as measured at 178 MHz [Jy].

Column [10]: Low frequency spectral index (178 – 750MHz).

Column [11]: Largest angular size [arcsec].

Column [12]: Reference for data. (1): Leahy & Perley (1991), (2): Mullin, Hardcastle & Riley (2006), (3): Gilbert et al. (2004), (4): Hardcastle et al. (1997), (5): Rudnick (1988), (6) Rudnick & Anderson (1990), (7): unpublished VLA archive, (8): Fernini, Burns & Perley (1997), (9): 3CRR atlas, (10): Bridle et al. (1994), (11): Katz & Stone (1997), (12): Leahy et al. (1997), (13): Taylor et al. (1995), (14): Clarke et al. (1992), (15): Fernini et al. (1993), (16): van Breugel & Day (1993), (17): Hough et al. (2004), (18): Black et al. (1992), (19): Roettiger et al. (1994), (20): Dennett-Thorpe et al. (1999)

angular distance of the lobe edge from the core. Θ_l and Θ_{LAS_l} are measured from the core to the 3σ contour (where σ is the off-source root mean square noise level) from the lowest resolution map available for the source. This criterion was chosen to give a consistent measure across the sample.

The procedure above introduces a potential source of bias, as the position of the 3σ contour will be dependent on observing resolution. Taking size measurements from the highest resolution map

available would minimize this effect but, as the low level emission from the lobes is often resolved out at high resolution, the extent of the large scale structure might be underestimated if this approach were taken. The Θ_l and Θ_{LAS_l} measurements have therefore all been made from the lowest resolution map available and a correction factor has been applied to compensate for resolution dependent beam-width smearing. The correction is that used by Gilbert & Riley (1999, hereafter G99). The maximum intensity, m , within two

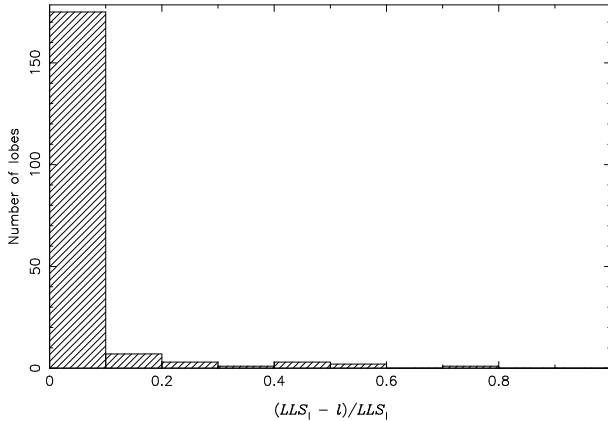


Figure 1. Histogram of $(LLS_1 - l)/LLS_1$, for the entire sample.

half-power beam widths of the apparent lobe edge (measured at the 3σ contour level) is found on the relevant axis. The half-width at the 3σ level of a Gaussian, of height m and with a half-power beam width equal to that of the restoring beam, can then be determined and subtracted from the apparent lobe length to correct for the effect of finite beam width.

All angular size measurements, Θ_{c-hs} , Θ_l and Θ_{LAS_1} , are converted respectively to linear sizes, $c-hs$, l and LLS_1 . The resolution correction factor is first subtracted from Θ_{LAS_1} and Θ_l ; that is, l and LLS_1 are quoted with the factor applied. (For this conversion the proper distance, R , is calculated using the ANGSIZ code².)

Although l and LLS_1 are not always the same within a lobe, as the core-hotspot axis may differ from that of the largest angular extent of the lobe from the core, in practice the difference between these two parameters is usually small, as illustrated in Fig. 1. In the following analysis LLS_1 is therefore used as the lobe size measurement and in the evaluation of the lobe axial ratio and lobe size asymmetry, both of which are discussed below in sections 2.2.2 and 2.2.3 respectively. The total linear source size, LLS_s , is defined as the sum of LLS_1 of both lobes.

In order to consider jet detectability (see section 4.1) we define the fractional observed lobe length, f_l , as the ratio of the observed extent of the lobe emission measured along the LLS_1 axis from the inner lobe edge at the 3σ contour to the lobe extremity, to LLS_1 .

2.2.2 Lobe axial ratio

The definition of the lobe width, Θ_w , is problematic as the morphologies of the lobes, both within individual sources and from source to source, are often very different. As Θ_w is to be used to determine the lobe axial ratio, a measurement representing the width at a set distance from the core, relative to the lobe extent, is appropriate. Not all sources have lobes extending back to the core but lobe emission is detected at least 2/3 along the core-hotspot axis from the core in all but 6 lobes. Θ_w has therefore been defined as the width of the lobe perpendicular to the core-primary hotspot axis as measured from the core at the point two-thirds along this axis. The 3σ contour is used to determine the lobe edge and measurements are made from the lowest resolution map available. This definition of lobe width was found to allow greater consistency in the measurement of Θ_w across the sample than other definitions that have

sometimes been used in the literature, such as the Gaussian FWHM (e.g., Leahy & Williams, 1994), given that the data here are high-resolution 8-GHz maps often with many beam widths across the lobes. While a Gaussian distribution represents a reasonable model of a slice taken through many lobes in the sample, a significant number would require multiple components to be fitted, as structure is detected in the lobe, which reduces the usefulness of this definition of width for our data.

The linear lobe width, w , is obtained from Θ_w and the lobe axial ratio, R_{ax} , is defined as LLS_1 over w .

2.2.3 Lobe size asymmetry

The lobe size asymmetry is defined by the fractional separation difference, x , as defined by Banhatti (1980):

$$x = \frac{D_1 - D_2}{D_1 + D_2} \quad (1)$$

where D_1 and D_2 are the two lobe sizes. D_1 may be taken as the longer lobe, giving x_{lobe} , or as the jet-side lobe if a jet is detected, giving x_{jet} . Previous studies have argued that using LLS_1 to define x_{lobe} and x_{jet} is preferable to $c-hs$ as from observations of multiple hotspots, hotspots are inferred to be transient features in the lobe (Scheuer 1995; Arshakian & Longair 2000, hereafter AL00). At the very least the physical region of the source to which hotspots correspond is ambiguous. Therefore, LLS_1 is used throughout to define x_{lobe} and x_{jet} .

2.2.4 Cores

The core measurements were obtained using the AIPS task JMFIT, which fits an elliptical gaussian model of between one and four components to a feature. One component was fitted and the peak intensity was taken as the core flux. As most cores in the sample were unresolved at all resolutions such a model fitted the data well; three measurements were made in this way (with different starting parameters) and averaged to give the final value. A corresponding error was obtained from the square root of the average of the squared formal errors returned from the fitting procedure. For around two thirds of the sample this error is less than 2 per cent of the core flux, so the calibration error (expected to be 2-3 per cent) will dominate. Errors quoted therefore correspond to 3 per cent of the core flux measurement, unless the formal error from JMFIT is greater, in which case the latter is quoted.

Core measurements have been taken from the highest resolution multi-array maps available for each source. For 7 sources, the core feature was either not detected or not well defined in the map and a 3σ upper limit for the core flux based on the local r.m.s. noise level was obtained. A few sources had variable cores – in these cases the core flux quoted is the lowest value measured. For details, see the papers in which the observations are presented as referenced in Table 1.

2.2.5 Jets

A jet feature is defined by criteria based on those of Bridle & Perley (1984). Thus, a jet is any feature that is

- (i) at least four times as long as it is wide;
- (ii) separable at high resolution from other extended structures (if any), either by brightness contrast or spatially (e.g. it should be

² <http://ascl.net/angsiz.html>

a narrow ridge running through more diffuse emission, or a narrow feature in the inner part of the source entering more extended emission in the outer part).

In some sources jets appear to bend, in particular as they reach the hotspot region. As discussed by Bridle et al. (1994), this could have consequences for beaming model analysis. Thus, following H98, we also define the straight jet, which fits the above criteria (i) and (ii) but also must be aligned with the compact radio core where it is closest to it (and is measured from the end closest the core along its length only while the deviation from a straight line is less than the jet radius), and the total jet, which fits the above criteria (i) and (ii) and has no alignment restriction (and includes the entire feature that is visible).

The method of measurement for both features is the same as that adopted by H98. The straight jet was measured using the AIPS task TVSTAT to find the integrated flux within the region containing the apparent jet emission, F_{obs} . A background flux correction was made by integrating two regions identical in size to the initial jet measurement on either side of the feature. The average of these, B_{obs} , was then subtracted from the jet measurement to give the observed jet flux, $J_{\text{obs}} = F_{\text{obs}} - B_{\text{obs}}$. In order to get the best estimate of J_{obs} , three values of jet flux were taken this way and averaged. The error in J_{obs} is almost always dominated by the ambiguity in defining the jet emission itself and so the errors quoted are half the measured maximum range of the three jet measurements made.

For the total jet TVSTAT is used to measure the integrated flux of the entire jet feature in the manner described for the straight jet, usually in straight sections that are then combined to give the total jet measurement. There are only 4 sources for which the more prominent feature defined by the straight jet criteria is not in the same lobe as that defined by the total jet criteria. Otherwise, the total jet measurement is often the same as the straight measurement (37 out of 65 sources with at least one possible or definite jet detection) or simply includes some further extension beyond a bend in the jet. In a few sources, the detected jet appears misaligned with the source axis such that the feature is thought to be associated with the flow downstream from some presumed bend in the beam. For these sources, the total jet measurement then corresponds to this feature.

Apparent jet-like features that fail the jet criteria are classified as possible jets and the fluxes of these are measured in the same way as definite jets. Typically these are features that are not prominent enough to be definite jets, though several fail on the length criterion. For those sources with a visible jet on both sides of the core, the brighter feature is defined as the jet, while the other jet is referred to as the counterjet. Where no jet emission is detected, an upper limit on the jet flux is estimated by measuring the integrated flux of a region ~ 2 restoring beam widths across the entire distance between the core and hotspot region. Background flux is corrected for in the same manner as for the definite and possible jets by taking two further integrated flux measurements either side of the initial region. However, if the flux associated with the central region is not the highest of the three, then the upper limit estimate is the positive difference between the central measure and the lower of the other two.

The straight jet measurement is used for considering beaming models and is used to define the jet side for parameters such as x_{jet} and hotspot ratios (defined in section 2.2.6). The total jet is used when jet morphology is considered. This is parametrized in the following way. The angular total jet length is defined to be the angular length of the feature identified as the total jet. The corresponding

angular jet position and jet termination are the angular separation of the base of the jet (that end of the feature nearest the core) and the tip of the jet (the end of the jet furthest from the core) from the core. The fractional jet length, f_{j_l} , fractional jet position, f_{j_p} and fractional jet termination, f_{j_t} are respectively the ratio of the linear jet length, position and termination to the lobe length, l . Note that the jet axis is not always the same as that along which the lobe length has been measured, giving a source of scatter in all three parameters.

2.2.6 Hotspots

Following H98, the hotspot is defined as any feature that is not part of a jet and that has a largest dimension smaller than 10 per cent of the main axis of the source as well as having a peak brightness greater than ten times the off-source noise. It must be separated from nearby peaks by a minimum falling to two-thirds or less of the brightness of the fainter peak. Where more than one such feature is observed, the most compact component is the primary hotspot while the remaining components are secondary hotspots.

Measurements of the hotspots were taken from the highest resolution multi-array map available for each source. The AIPS task JMFIT was used to give an integrated flux value as well as the major and minor axes, Θ_{maj} and Θ_{min} , the half-widths of the fitted Gaussian. The angular hotspot size, Θ_h , was then defined as the arithmetic mean of Θ_{maj} and Θ_{min} . The average angular hotspot size, $\Theta_{h_{av}}$, is defined as the arithmetic mean of the sizes of the primary hotspots in both lobes.

Fitting was carried out several times for each feature with varying starting parameters and similar results were generally obtained. However, for some of the most highly resolved features at lower redshift this was not the case and an alternative to JMFIT was used. If the feature was too resolved, or convergence could not be achieved in flux within a factor of 1.5 either way, a manual measurement was made. Fluxes were estimated by integration from the maps with TVSTAT; background emission was taken into account by integrating over a surrounding region, normalising the flux to an area equivalent to that of the hotspot and subtracting. In order to make size measurements, the FWHM was estimated from slices taken through the feature. Errors have not been quoted for hotspot flux density or size since the parameters are subjective: the dominant error will derive from the ambiguity in determining the hotspot region.

The linear hotspot size, h , is obtained from Θ_h and the fractional hotspot size, f_h , is the ratio of h to LLS_l .

2.2.7 Hotspot recession

Three recession parameters are defined, η , ζ and Δ . η is the lobe hotspot recession: the ratio of $c - hs$ to LLS_l for each lobe. ζ is the source hotspot recession: the ratio of the sum of $c - hs$ for the two lobes to the total source size, LLS_s . Δ quantifies the recession asymmetry in a single source and is defined as the ratio of the smaller to the larger value of η .

2.3 Observing frequency and prominence

The total source flux observed at 178 MHz is K-corrected using the corresponding low frequency spectral index (both parameters are taken from LRL), giving S_{total} at 178 MHz. S_{total} is used to obtain

the source luminosity, P_{178} , using the relation

$$P_{178} = R^2(1+z)^2 S_{\text{total}} \quad (2)$$

(where R is the proper distance). The source luminosity is determined from the low-frequency source flux as this ought to be dominated by the steep-spectrum, unbeamed emission associated with the lobes, so that little contribution should be made by any relativistic beaming.

All the flux densities of compact features of the sources discussed above are extrapolated from the observed flux density to a common frequency of 8.4 GHz

$$S_{8.4} = S_{\text{v}_{\text{obs}}} \left(\frac{\text{v}_{\text{obs}}}{8.4} \right)^\alpha \quad (3)$$

and then K-corrected to an emitted frequency

$$S = S_{8.4}(1+z)^{\alpha-1} \quad (4)$$

where v_{obs} is the observing frequency in GHz and α the spectral index, assumed to be 0 for core features and 0.5 for jet and hotspot features. These flux densities are converted to luminosities using equation (2).

The source luminosity is used as a normalization factor for these core, hotspot and jet luminosities to define prominence parameters. The core, hotspot and straight jet prominence (p_c , p_h , p_j) are respectively the ratio of the core, hotspot and straight jet luminosity to P_{178} . (Note that this normalization factor is different from that used by H98, so that our prominences are different from theirs.)

A glossary of all parameters that have been defined in this section (along with others that will be defined subsequently) is given in Table 2.

2.4 Effective observing resolution

The sample extends to a redshift of 1. While the aim of the observing program was to obtain data of a consistent quality across the sample, there are inevitably instrumental limits in achieving this. At increasing redshift the angular resolution relative to the source size must decrease for a fixed beam width, so that more distant sources are observed at increasing linear scales for a given source size. One key parameter here is the number of restoring beams across the source, which we refer to throughout the paper as the effective observing resolution. The high-resolution effective observing resolution is defined as the ratio of the restoring beam size of the highest-resolution map for each source to LLS_s ; the low-resolution effective observing resolution is defined similarly but using the restoring beam size from the lowest-resolution map.

In Fig. 2 the linear source size, LLS_s , is plotted against the *high-resolution* effective observing resolution for the sample, to highlight the range in this quantity that corresponds to the sample's high-resolution maps, since this is the more important quantity as regards source properties. It can be seen that there is a range of effective observing resolutions associated with the sources; this may have consequences, in particular, for the consideration of jet and hotspot properties. In the following sections, in which we discuss the lobe, core, jet and hotspot properties, we consider the limitations imposed by our observing strategy as well as trends with power, redshift and size.

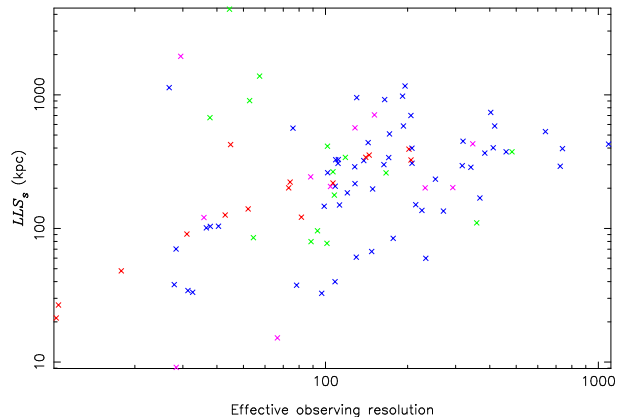


Figure 2. The largest linear source size, LLS_s , plotted against the high-resolution effective observing resolution. Green: low excitation radio galaxies, blue: narrow line radio galaxies, magenta: broad line radio galaxies and red: quasars (on-line colour version).

3 LOBES

3.1 Lobe size

3.1.1 Observational effects

Observational effects in lobe properties may be introduced by using the 3σ contour as the criterion for defining Θ_{LAS} and Θ_l and this is addressed by the application of a correction factor, as described in section 2.2.1.

3.1.2 Trends with P_{178} and z

There is no straightforward physical correlation to be expected between the beam kinetic power, the lobe size and P_{178} , although sources are believed to decrease in luminosity as they expand and age (Fanti et al., 1995; Kaiser & Alexander, 1997; Kaiser, Dennett-Thorpe & Alexander, 1997; Blundell, Rawlings & Willott, 1999). The higher-luminosity sources may be observed at an earlier stage in their lifecycle as sources fall below the sample flux limit as they move through the luminosity-source linear size ($P-D$) diagram; statistically, therefore, they may be expected to be smaller. In a flux-limited sample there is a $P-z$ degeneracy, so any tendency for LLS_s to decrease with increasing P_{178} may also be seen as a trend in redshift.

In Fig. 3 it can be seen that LLS_s tends to be smaller for the higher luminosity sources; a similar but weaker effect is shown in the plot of LLS_s against redshift in Fig. 4. Spearman rank correlation tests give $r_s = -0.31$ and -0.29 respectively for these two trends, implying a correlation significant at better than the 99 per cent confidence level. However, comparing subsamples of sources defined with a 178-MHz luminosity cutoff, $P_c = 5 \times 10^{26} \text{ W Hz}^{-1} \text{ sr}^{-1}$, inclusive of all spectral classes, a W-M-W test does not show a significant difference in size between the high and low luminosity populations; we can conclude that any trends with source size found in other parameters for the sample should not then be systematically biased across the power or redshift range.

The value of 178-MHz luminosity, P_c , chosen above gives the minimum overlap between the quasar and BLRG populations: these can be seen from Figs 3 and 4 to occupy different ranges of luminosity and redshift, with the higher-luminosity quasar population found at higher redshift. Throughout the paper we therefore make comparisons between the NLRG and the BLRG, Q and

Table 2. Glossary of symbols used.

Symbol	Parameter	Reference
S_{178}	total source flux as measured at 178 MHz	section 2.1
S_{total}	K-corrected total source flux density, as measured at 178 MHz	section 2.3
P_{178}	source luminosity, as measured at 178 MHz	section 2.3
α	spectral index	section 2.3
Θ_{c-hs}	angular core-primary hotspot separation	section 2.2.1
Θ_l	angular lobe length	section 2.2.1
Θ_{LAS_l}	largest angular lobe size	section 2.2.1
Θ_w	angular lobe width	section 2.2.2
$c-hs$	linear core-primary hotspot separation	section 2.2.1
l	linear lobe length	section 2.2.1
LLS_l	largest linear lobe size	section 2.2.1
LLS_s	largest linear source size	section 2.2.1
w	linear lobe width	section 2.2.2
f_l	fractional observed lobe length	section 2.2.1
R_{ax}	lobe axial ratio	section 2.2.2
x_{lobe}	fractional separation difference, as defined by the longer lobe	section 2.2.3
x_{jet}	fractional separation difference, as defined by jet side	section 2.2.3
F_{obs}	measured jet flux	section 2.2.5
B_{obs}	jet background flux correction	section 2.2.5
J_{obs}	background-corrected jet flux	section 2.2.5
f_{jl}	fractional jet length	section 2.2.5
f_{jp}	fractional jet position	section 2.2.5
f_{jt}	fractional jet termination	section 2.2.5
Θ_{maj}	hotspot major axis	section 2.2.6
Θ_{min}	hotspot minor axis	section 2.2.6
Θ_h	hotspot size	section 2.2.6
Θ_{hav}	average primary hotspot size	section 2.2.6
h	linear hotspot size	section 2.2.6
f_h	fractional hotspot size	section 2.2.6
η	lobe hotspot recession coefficient	section 2.2.7
ζ	source hotspot recession coefficient	section 2.2.7
δ	hotspot recession asymmetry	section 2.2.7
p_c	core prominence	section 2.3
p_h	hotspot prominence	section 2.3
p_j	straight jet prominence	section 2.3
P_c	luminosity cutoff of $5 \cdot 10^{26} \text{ W Hz}^{-1} \text{ sr}^{-1}$	section 3.1.2
θ_c	hypothetical angular spectral class cutoff	section 3.1.3

LERG classes by dividing the NLRG data into low- and high-luminosity samples at P_c . This gives a low-luminosity and high-luminosity NLRG subsample of 19 and 38 sources respectively: the low-luminosity sample is very similar in luminosity to (and contains many of the same sources as) the $z < 0.3$ 3CRR/3CR sample used by H98.

3.1.3 Unification

Considering only those classes included in the standard FR II unification scheme (BLRGs, NLRGs and Qs) the BLRGs constitute 31 ± 11 per cent of the sample at low luminosity and the Qs 26 ± 7 per cent of the sample at high luminosity (assuming errors of \sqrt{N}), so the proportions are not significantly different for the two subsamples. This lends support to a model in which the BLRGs and

Qs are equivalent populations and also implies no significant variation in the opening angle of the torus.

The opening angle of the torus can be estimated from the number counts of the Qs, BLRGs and NLRGs, assuming that the source axis must be viewed at an angle less than the torus angle for the broad line emission to be detected. For the simple unification model, this gives θ_c as a parameter that divides the classes, with $\theta \leq \theta_c$ for the Qs and BLRGs and $\theta > \theta_c$ for the NLRGs, where θ is the angle the source axis makes with the observer's line-of-sight. The expected fraction of broad emission line objects detected is $P(\leq \theta_c) = 1 - \cos \theta_c$. This implies that for the lower luminosity bin $\theta_c \sim 51^\circ$, while for the higher luminosity bin $\theta_c \sim 45^\circ$, consistent with the findings of Barthel (1989). An average value $\theta_c = 48^\circ$ will be used hereafter.

According to the unification scheme, the Q and BLRG sources should be orientated closer to the observer's line-of-sight than the NLRG sources. Evidence consistent with this hypothesis would be a difference in the size distributions of the spectral classes of the Qs, BLRGs and NLRGs consistent with projection effects. The LERGs are believed to be randomly orientated with respect to the observer.

The relation between the true physical size, LLS'_s , and observed source lengths, LLS_s , is given by

$$LLS_s \approx LLS'_s \sin \theta \quad (5)$$

(the relation is not exact as the sum of the two lobes does not necessarily give a common axis). The ratio of the expected median size for the broad and narrow line sources can be predicted from the ratio of the median θ ,

$$\frac{\langle LLS_{s,Q,B} \rangle}{\langle LLS_{s,N} \rangle} = \frac{\sin(\langle \theta_{Q,B} \rangle)}{\sin(\langle \theta_N \rangle)} \quad (6)$$

where $\langle X \rangle$ denotes the median value of parameter X and $\langle \theta \rangle$ is evaluated by integrating over the appropriate θ range. Using $\theta_c = 48^\circ$, $\langle \theta_{Q,B} \rangle = 33^\circ$ and $\langle \theta_N \rangle = 70^\circ$, a predicted value of $\langle LLS_{s,Q,B} \rangle / \langle LLS_{s,N} \rangle = 0.57$ is obtained. The $\langle LLS_s \rangle$ values for the Qs, BLRGs and NLRGs are given in Table 3; the data for the LERGs are included for comparison. The ratios of Q and BLRG median values to those of the NLRGs in the respective luminosity bins is 0.73 and 0.70; if we take all the objects together without binning by luminosity the ratio is 0.70. A W-M-W test does not show that this is statistically significant. According to the model, LERG sources are randomly orientated so there is no predicted difference between them and the low luminosity NLRG and BLRG population, that is, $\langle LLS_{s,B,N} \rangle / \langle LLS_{s,E} \rangle = 1$ assuming that they have the same physical size distribution. A ratio of 0.93 is found in the data, but a W-M-W test does not suggest that the LERGs are significantly smaller. (This is in contrast to the finding in H98 that LERGs were significantly smaller than the BLRGs and NLRGs in the low redshift sample they studied. That sample included those sources of this paper's sample with $z < 0.3$ along with a number of others. The difference may well arise from the definition of source size used; H98 used the largest linear source size as obtained from the largest angular source size, whereas here LLS_s is used, the sum of the largest linear lobe size for both lobes. For a good proportion of the sources in this sample with $z < 0.3$ the largest angular source size is greater than LLS_s . In addition, the sample of H98 excluded a number of giant sources that we include here.)

Whilst these results are in the sense expected in the unification scheme, the effect is weaker than expected and no statistically significant difference in source size between the Qs, BLRGs and NLRGs is found.

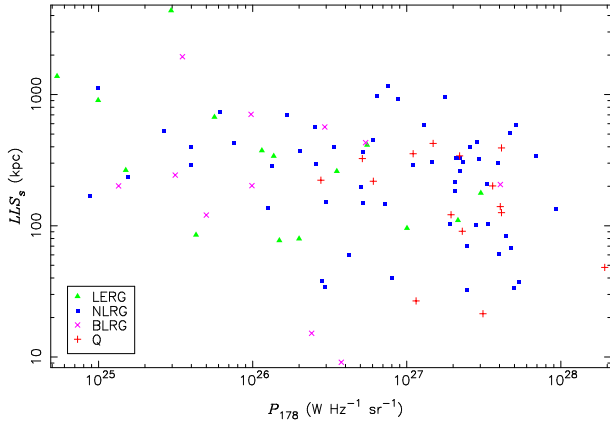


Figure 3. The largest linear source size, LLS_s , plotted against the source luminosity as measured at 178 MHz, P_{178} .

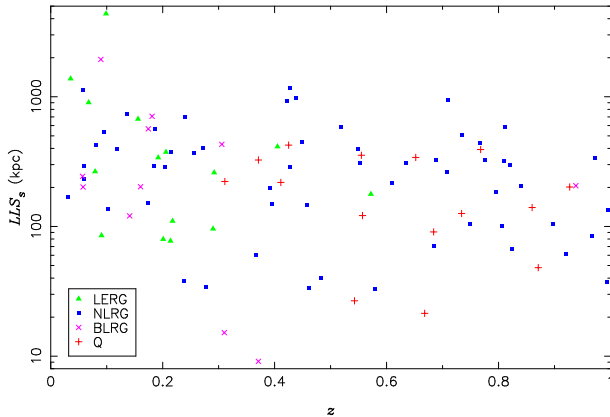


Figure 4. The largest linear source size, LLS_s , plotted against redshift, z .

Table 3. The median largest linear source size, $\langle LLS_s \rangle$, for each of the spectral class distributions.

Spectral class	$\langle LLS_s \rangle$	Spectral class	$\langle LLS_s \rangle$	$\langle LLS_s \rangle$ ratio
Q	201	NLRG, high $P_{178\text{MHz}}$	275	0.73
B	206	NLRG, low $P_{178\text{MHz}}$	295	0.70
Q and BLRG	204	NLRG	292	0.70
LERG	270	BLRG and low $P_{178\text{MHz}}$	289	0.93

3.2 Lobe axial ratio

3.2.1 Observational effects

Both Θ_w and Θ_{LAS_1} are taken from the lowest resolution map available with the lobe edge determined by the 3σ contour. However, as discussed in section 3.1.1, this will be affected by observing resolution and sensitivity. In the case of Θ_{LAS_1} a correction factor was applied in an attempt to compensate for any systematic bias introduced by observing resolution effects. Whilst this factor is necessarily only an order-of-magnitude correction, we felt that, as in almost all sources the lobe extremity is associated with a bright emission peak, the effect of beam-width smearing on the source structure is large enough that the application of the correction factor as defined is useful.

In the case of Θ_w , however, the emission at the lobe edges is usually at a low level and the validity of such a correction is less clear. For example, orientation effects could affect the observed lobe width, with those sources observed with their axes closer to our line-of-sight having more extensive lobes if source viewing an-

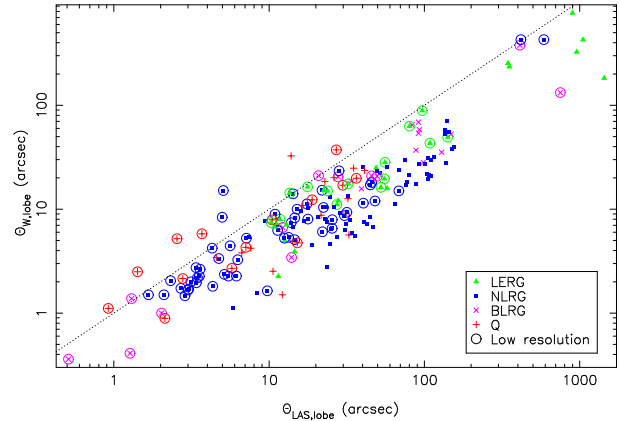


Figure 5. The angular lobe width, Θ_w , plotted against the resolution-corrected angular lobe size, Θ_{LAS_1} , binned by low-resolution effective observing resolution. Circled points: low-resolution effective observing resolution ≤ 40 . The dotted line is the line of $\Theta_w = \Theta_{LAS_1}$.

gle allows a greater depth of emission to be detected near the lobe edges. This effect, if it is significant, cannot be compensated for by the correction factor in the way that we have defined it for the lobe lengths. Accordingly, we have chosen not to apply any correction factor to Θ_w .

In Fig. 5 we plot the angular lobe width against the resolution-corrected angular largest lobe size, binned by *low-resolution* effective observing resolution. There is a tendency for those sources observed at relatively low resolution, that is with ≤ 40 restoring beams across the source, to have wider lobes. Dividing the lobe width data points into two subsamples based on observing resolution, using a cutoff of 40 low-resolution restoring beams across the source, a W-M-W test suggests this is significant above the 99.9 per cent confidence level. Furthermore, when we consider the R_{ax} values themselves and divide them into two samples in the same way, a W-M-W test shows that R_{ax} is significantly higher in sources observed at high resolution compared to those observed with an effective observing resolution of 40 or less, at above the 99.9 per cent confidence level. The R_{ax} data, therefore, seem to be affected by observing resolution.

3.2.2 Trends with P_{178} , z and size

A greater proportion of sources observed at low resolution are found at high redshift, so that the high redshift sample may have a systematic bias toward lower R_{ax} values. Another effect to consider is the known correlation between spectral index and radio power or redshift; the hotspots and lobes in higher-redshift higher-power sources have steeper spectra, particularly at high frequencies (e.g., Laing & Peacock 1980; Blundell, Rawlings & Willott 1999). This correlation would mean that for high-redshift sources the low brightness lobe emission is harder to detect, resulting in smaller w values (and hence higher corresponding R_{ax}) for luminous sources. Dividing the R_{ax} distribution by P_{178} (using P_c) and z (using a cutoff of 0.5), a K-S test showed no significant differences in the distribution of R_{ax} across the power and redshift range. In Figs 6 and 7 we plot R_{ax} (for each lobe) against redshift and source luminosity respectively.

The plot of R_{ax} against LLS_1 in Fig. 8 shows that there is a trend with source size. The distribution appears to change at $LLS_1 \sim 100$ kpc, with a much larger range in R_{ax} found above this size. A

W-M-W test shows that R_{ax} is significantly smaller in lobes with $LLS_1 < 100$ kpc at above the 99.9 per cent confidence level, for sources of all spectral classes.

In a self-similar expansion model in which all sources in a sample are subject to self-similar growth throughout their lifetime, R_{ax} should be independent of the lobe size. This is clearly not borne out by the data. In fact it is possible that a source only grows self-similarly in its early phases, on scale sizes of the order of that of the associated galaxy or its hot-gas halo (e.g. Hardcastle & Worrall 2000); the data here lend support to this picture.

3.2.3 Unification

The observed R_{ax} should be lower than the true physical value due to the projection of the source length in the plane of the sky, while the width should be less affected, notwithstanding any orientation effects on lobe detectability as discussed in section 3.2.1. Assuming w is unaffected by orientation, the effect of projection on R_{ax} is the same form as that for LLS_s (equation 5), that is

$$R_{\text{ax}} = R'_{\text{ax}} \sin \theta, \quad (7)$$

where the prime indicates the true physical value of the parameters and θ is the angle subtended by the LLS_s axis with the observer's line-of-sight.

The median R_{ax} , $\langle R_{\text{ax}} \rangle$, is given for the different spectral classes in Table 4. Unification predicts the same ratio (~ 0.6) between the broad and narrow line spectral classes as for $\langle LLS_s \rangle$ (given the model in equation (7) and ignoring scatter introduced by deviation of the lobes from the common axis). For the sample data, $\langle R_{\text{axQ}} \rangle / \langle R_{\text{axN}} \rangle = 0.69$, while $\langle R_{\text{axB}} \rangle / \langle R_{\text{axN}} \rangle = 0.75$.

The difference in R_{ax} between the Qs and high luminosity NLRGs is statistically significant (at the 99.6 per cent confidence level with a W-M-W test) whilst that between the BLRGs and low luminosity NLRGs is not, though the difference between the low-power spectral classes is in the sense expected for unification. So are there intrinsic differences between the Qs and high power NLRGs that have no correspondence in the low luminosity sources? This may not be the case if some effect leads to an observational bias that masks significant differences in R_{ax} between the BLRGs and low-power NLRGs – for example, if lobes were more difficult to detect in these low-power sources compared with high-power ones. However, despite the evidence that observing resolution does affect R_{ax} (section 3.2.1), we concluded in section 3.2.2 that there was no evidence that this results in a systematic bias in lobe detectability across the power range.

While the tendency for Qs to have lower R_{ax} than high-power NLRGs is consistent with projection effects, the orientation arguments predict that this should be the case *as a result of* their lower values of LLS_1 . In fact we found no significant difference in lobe length between the Qs and high luminosity NLRGs, which might suggest that the Qs are associated with lower R_{ax} because they have intrinsically broader lobes. A W-M-W test does not confirm that this is the case, however.

In Fig. 9 we plot w against LLS_1 for the different spectral classes. From this plot it would appear that there is a tendency for the points corresponding to the broad line objects to lie to the left of those of the narrow line objects – in other words, there is a tendency for Qs and BLRGs to have smaller LLS_1 with respect to NLRGs of a similar w . This would suggest that differences are consistent with projection effects, although the LLS_1 values in Qs and BLRGs are not significantly lower than those in NLRGs. Our interpretation is therefore that the statistically lower R_{ax} found in

Table 4. The median lobe axial ratio, $\langle R_{\text{ax}} \rangle$, for each of the spectral class distributions.

Spectral class	$\langle R_{\text{ax}} \rangle$	Spectral class	$\langle R_{\text{ax}} \rangle$	$\langle R_{\text{ax}} \rangle$ ratio
Q	1.65	NLRG, high $P_{178\text{MHz}}$	2.38	0.69
B	1.93	NLRG, low $P_{178\text{MHz}}$	2.56	0.75
Q and BLRG	1.75	NLRG	2.49	0.70
LERG	1.90	BLRG and low $P_{178\text{MHz}}$	2.40	0.79

Qs is consistent with projection effects; the lack of a corresponding trend for BLRGs is not accounted for, though it is not strong evidence against unification in the lower-power subsample. Fig. 10 shows that a number of the low-power sources with low effective observing resolution correspond to either particularly small or particularly large sources and it is possible that the effects of observing resolution are more important for the BLRGs, though this is not clearly so.

As for the lobe size, we would predict no significant difference in R_{ax} between the LERGs and low luminosity NLRGs and BLRGs, if LERGs have the same intrinsic R_{ax} distribution. A K-S test finds no significant difference between the R_{ax} distributions of the LERG and combined BLRG and low power NLRG populations.

3.3 Lobe size asymmetry

3.3.1 Trends with P_{178} , z and size

The resolution correction factor applied to the LLS_1 data, as discussed in section 3.1.1, should compensate for systematic bias in lobe size asymmetry that might be introduced by observing resolution. The fractional separation difference defined in terms of the longer lobe, x_{lobe} , is plotted as a function of redshift, luminosity and source size in Figs 11, 12 and 13 respectively. There is no trend in x_{lobe} with redshift but there is a tendency for the high luminosity and smaller sources to have greater asymmetries.

A trend in x_{lobe} with redshift might have suggested environmental differences at different epochs; a tendency for greater asymmetries in higher power/smaller sources only could be consistent with asymmetries being imposed by environmental differences early in the source's development, if these sources are expected to be generally younger. That is, if relative environmental differences are not so great further out from the central engine the source's perceived asymmetry may be dominated by effects introduced while the source is still small; in this case the fractional asymmetry may decrease as the source expands, as any asymmetry represents a decreasing fraction of the source size.

Broad-band studies of radio galaxies have demonstrated that in many cases the detected optical and/or infrared continuum emission from the host galaxy is aligned with the radio axis (Chambers, Miley & van Breugel, 1987; McCarthy et al., 1987), a phenomenon known as the 'alignment effect'. This effect has been shown to be strong in sources at redshifts $\gtrsim 0.6$, but less so for lower redshift samples. The main processes implicated in the creation of the alignment effect are photoionization from the central AGN and shock ionization from the passage of the jet or lobes. Spectroscopic studies have suggested that the photoionization mechanism dominates in more evolved, larger sources but in smaller sources (especially those for which the radio size of the sources is comparable to the emission line region) the shock mechanism becomes important. This implies that source age is a key factor when considering the extent to which the radio source will affect its environment, with younger, less-evolved sources expanding out through the host galaxy and gas environment and directly affecting

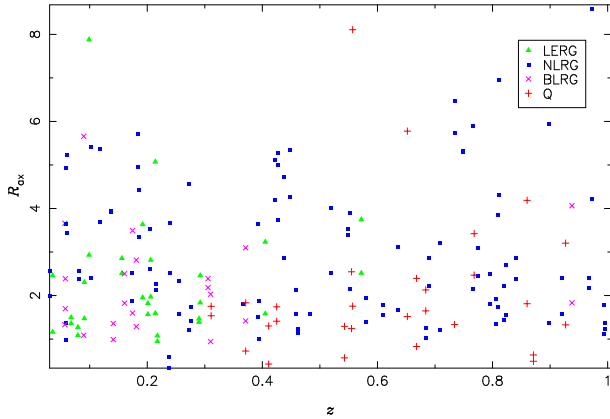


Figure 6. The lobe axial ratio, R_{ax} , plotted against redshift, z (two points per source).

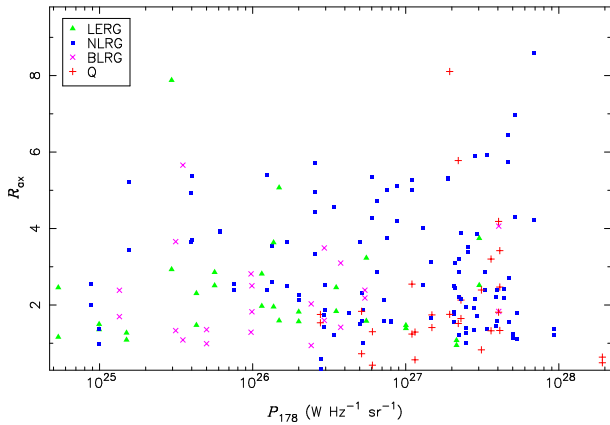


Figure 7. The lobe axial ratio, R_{ax} , plotted against source luminosity at 178 MHz, P_{178} , (two points per source).

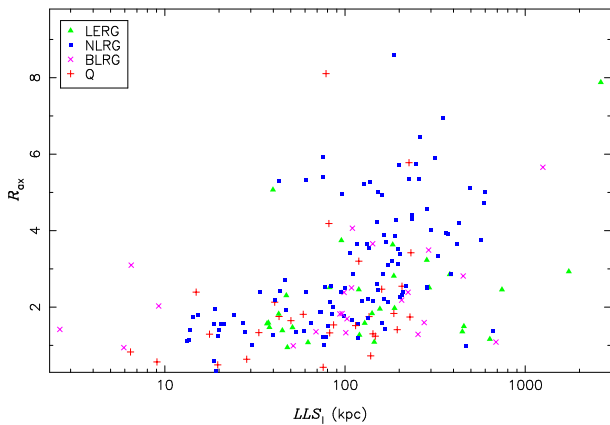


Figure 8. The lobe axial ratio, R_{ax} , plotted against the largest linear source size, LLS_1 , (two points per source).

their kinematics (e.g., Inskip et al. 2002; Privon et al. 2008). But the study of Inskip et al., which was made using multiple flux-limited samples in order to break the redshift-luminosity degeneracy, has suggested that the alignment depends on redshift as well as power, implying that environmental differences at different epochs do contribute to the overall picture.

The present sample cannot directly inform these latter results, as the redshift-luminosity degeneracy is not broken here. In fact, the tendency for asymmetry to be greater for higher power, smaller

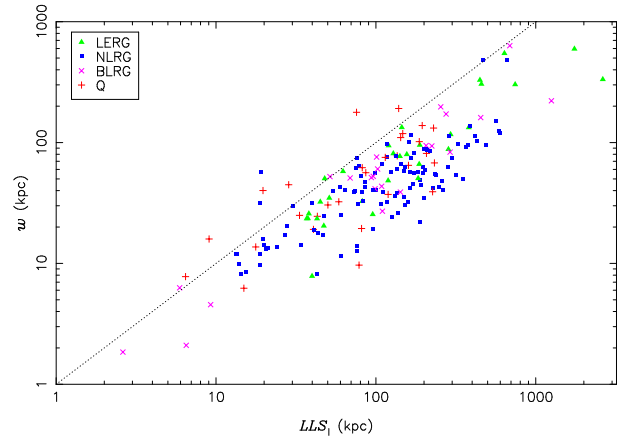


Figure 9. The linear lobe width, w , plotted against the largest linear lobe size, LLS_1 . The dotted line is the line of $w = LLS_1$.

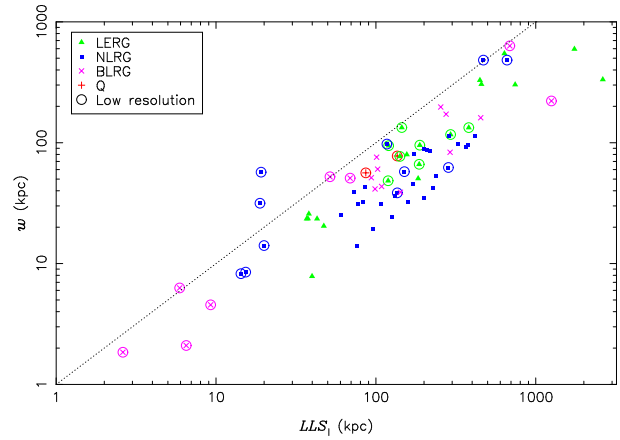


Figure 10. The linear lobe width, w , plotted against the largest linear lobe size, LLS_1 , for the low power subsample. Circled points: low-resolution effective observing resolution ≤ 40 . The dotted line is the line of $w = LLS_1$.

sources in this sample is not a result that contradicts or confirms any study of the alignment effect; binning the entire sample data by luminosity (using P_c) and source size (taking a cutoff of 200 kpc, corresponding to 100 kpc in lobe size, a somewhat arbitrary choice based on the result of a trend in R_{ax} with lobe size discussed in section 3.2.2), K-S tests indicate that the differences in the distributions of x_{lobe} across both the luminosity and size ranges are not significant.

3.3.2 Unification and beaming

The median x_{lobe} for the different spectral classes, $\langle x_{lobe} \rangle$, are given in Table 5. It can be seen that the Qs are more asymmetric than the high luminosity NLRGs; a W-M-W test shows that the difference is significant at the 99.7 per cent confidence level. The $\langle x_{lobe} \rangle$ of the BLRGs and the low luminosity NLRGs are not significantly different statistically and a K-S test does not show any difference in the distribution of the combined population of BLRGs and low-power NLRGs with respect to that of the LERGs. These findings are generally consistent with those of H98 (with respect to the low luminosity sources) and Best et al. (1995; with respect to the high luminosity subsample), though both these studies defined x_{lobe} using $c - hs$.

In the case of the former result, Best et al. suggested that rela-

tivistic effects might contribute to the greater asymmetry of Qs relative to the corresponding NLRGs. If this were the case, we would expect that the jet side would correlate with the longer lobe side. The fractional separation difference defined by jet side, x_{jet} , uses the value of LLS_1 on the straight jet side as D_1 and LLS_1 on the counterjet side as D_2 . AL00 have studied the observed distribution of x_{jet} for a sample of 3CR FR II sources that includes the sources in this sample in addition to a number of objects at $z > 1$. They introduce an asymmetry parameter, ε , which is used to quantify the degree to which relativistic effects contribute to the observed distribution of x_{jet} as opposed to intrinsic and/or environmental effects. The asymmetry parameter is defined as

$$\varepsilon = 1 - 2 \frac{N(-FRII)}{N(+FRII)} \quad (8)$$

where $N(-FRII)$ and $N(+FRII)$ are the numbers of sources with positive and negative x_{jet} values. AL00 argued that an even distribution of positive and negative x_{jet} about zero, giving $\varepsilon = -1$, implies that relativistic effects are not a significant factor in the distribution. Where around 2/3 of the sample objects have positive x_{jet} values, $\varepsilon \sim 0$, which implies that relativistic effects are as significant as intrinsic/environmental ones. As relativistic effects become more important ε would become increasingly positive. For their sample AL00 found an asymmetry parameter of -0.07 ± 0.22 , for all the sources. For the radio galaxies the result was -0.3 ± 0.32 and for quasars, 0.33 ± 0.36 . They concluded that the effects of relativistic motion on the observed lobe size asymmetry distribution were not negligible and that they were more important to the observed quasar asymmetries than to the radio galaxies, consistent with unification models.

Here the sample is essentially the same as that of AL00 except for the exclusion of those objects at $z > 1$. The data have been re-considered, however, using only the jet-side information obtainable from the sample maps. Where a definite or possible straight jet is detected, this is taken as the jet side and no other information such as the depolarization asymmetry associated with the source is used. When determining x_{jet} in this way, it must be borne in mind that the exclusion of those sources with no jet detections may bias the data.

x_{jet} is plotted against P_{178} in Fig. 14. Considering all sample sources with at least one definite or possible straight jet, regardless of spectral class, the jet-side lobe is the longer lobe in 49 per cent of the sources (using LLS_j). BLRGs show the strongest apparent correlation of jet side and the longer lobe with 7 out of 8 sources having positive x_{jet} values; a marginally significant tendency at the 96.5 per cent confidence level. Qs, NLRGs and LERGs do not have any significant tendency for positive x_{jet} values. The distribution corresponds to an asymmetry parameter of $\varepsilon = -1.06$ for the combined Qs, BLRGs and NLRGs sample, $\varepsilon = 0.08$ for the combined quasar and BLRG population and $\varepsilon = -1.86$ for the NLRGs, suggesting that relativistic effects make a greater contribution to the observed asymmetry for Qs and BLRGs than for NLRGs, which is in line with the prediction of unification. This is consistent with the results of AL00, although the evidence for relativistic effects making a significant contribution to the x_{jet} distribution overall is weaker for this sample.

In Fig. 15, x_{jet} is plotted against LLS_s . There is an apparent difference in the x_{jet} distribution for smaller sources, ($LLS_s \lesssim 200$ kpc), with fewer negative values: x_{jet} is positive in 57 per cent of sources with $LLS_s \leq 200$ kpc; a binomial test shows the tendency for x_{jet} to be positive in the smaller sources is only weakly significant (although it can be noted that only one broad-line source has a

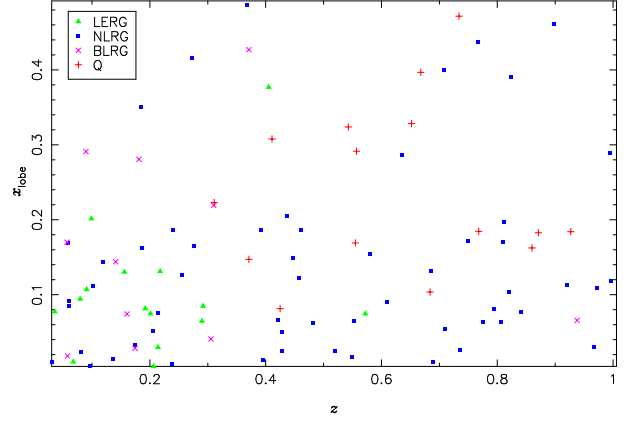


Figure 11. The fractional separation difference as defined by the longer lobe side, x_{lobe} , plotted against redshift, z .

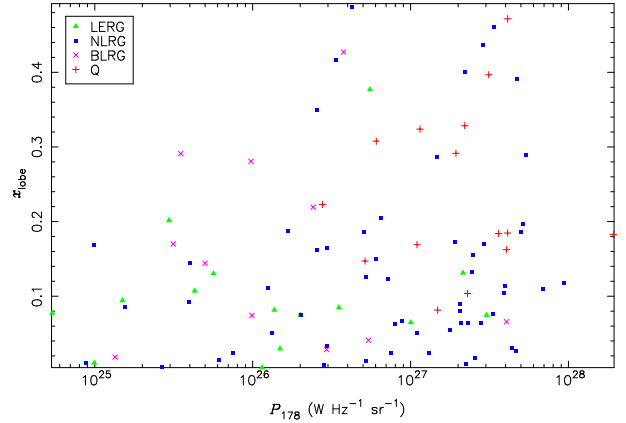


Figure 12. The fractional separation difference as defined by the longer lobe side, x_{lobe} , plotted against source luminosity at 178 MHz, P_{178} .

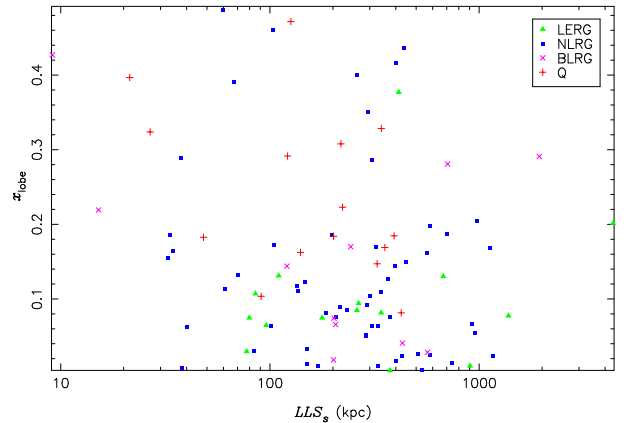


Figure 13. The fractional separation difference as defined by the longer lobe side, x_{lobe} , plotted against the largest linear source size, LLS_s .

negative value). A K-S test shows no significant difference between the large and small source x_{jet} distribution.

Table 6. Summary of jet and hotspot detections for the sample

Source	Class	Straight jets		Hotspots		Source	Class	Straight jets		Hotspots		Source	Class	Straight jets		Hotspots	
		N lobe	S lobe	N lobe	S lobe			N lobe	S lobe	N lobe	S lobe			N lobe	S lobe	N lobe	S lobe
4C12.03	E	J	PCJ	1	1	3C196	Q	none	none	1	1	3C289	N	none	none	0	1
3C6.1	N	none	none	1	1	3C200	N	none	J	1	1	3C292	N	none	none	1	1
3C16	E	PJ	PCJ	0	1	4C14.27	N	PJ	PCJ	1	1	3C295	N	none	none	1	1
3C19	N	none	PJ	1	1	3C207	Q	none	J	2	1	3C299	N	none	none	3	1
3C20	N	J	none	1	1	3C215	Q	none	PJ	1	4	3C300	N	J	none	1	2
3C22	B	J	none	2	2	3C217	N	none	none	2	1	3C303	B	J	none	1	1
3C33	N	PCJ	PJ	1	2	3C216	Q	none	none	1	1	3C319	E	none	none	1	0
3C33.1	B	none	J	1	1	3C219	B	PCJ	J	1	1	3C321	N	PJ	none	1	1
3C34	N	PJ	PCJ	1	1	3C220.1	N	J	none	2	1	3C325	Q	PJ	none	1	2
3C35	E	none	none	1	0	3C220.3	N	none	none	1	1	3C326	B	none	none	0	1
3C41	N	none	J	1	1	3C223	N	PJ	PCJ	1	1	3C330	N	none	none	1	3
3C42	N	none	none	1	1	3C225B	N	none	none	1	1	3C334	Q	PCJ	J	2	1
3C46	N	none	PJ	2	2	3C226	N	none	none	1	1	3C336	Q	none	J	3	1
3C47	Q	none	J	1	1	4C73.08	N	none	none	1	1	3C341	N	none	J	0	0
3C55	N	none	PJ	1	2	3C228	N	none	J	1	2	3C337	N	none	PJ	1	1
3C61.1	N	none	none	1	0	3C234	N	J	none	1	1	3C340	N	none	none	1	1
3C67	B	PJ	none	2	1	3C236	E	PJ	none	0	1	3C349	N	none	PJ	1	1
3C79	N	none	none	3	3	4C74.16	N	none	J	1	1	3C351	Q	PJ	none	1	1
3C98	N	J	none	1	1	3C244.1	N	PJ	none	2	1	3C352	N	J	none	2	0
3C109	B	none	PJ	1	1	3C247	N	none	none	1	1	3C381	B	none	none	1	1
4C14.11	E	PJ	none	2	1	3C249.1	Q	J	none	4	1	3C382	B	J	none	1	1
3C123	E	none	none	1	1	3C254	Q	none	none	1	1	3C388	E	none	J	1	1
3C132	E	none	PJ	1	1	3C263	Q	none	J	1	1	3C390.3	B	J	none	1	1
3C153	N	PCJ	PJ	1	3	3C263.1	N	none	none	1	1	3C401	E	none	J	1	1
3C171	N	CJ	J	1	1	3C265	N	PJ	none	1	1	3C427.1	E	PJ	none	2	1
3C172	N	none	none	1	2	3C268.1	N	none	none	2	1	3C433	N	J	none	0	4
3C173.1	E	J	none	1	1	3C268.3	B	none	none	1	1	3C436	N	none	J	3	1
3C175	Q	none	J	1	2	3C274.1	N	none	PJ	1	1	3C438	E	J	none	1	1
3C175.1	N	none	PJ	1	1	3C275.1	Q	J	none	1	1	3C441	N	J	none	1	1
3C184	N	none	none	3	1	3C277.2	N	none	PJ	3	1	3C452	N	CJ	J	1	1
3C184.1	N	PJ	none	1	1	3C280	N	none	none	1	1	3C455	Q	none	none	1	1
DA240	E	none	PJ	1	2	3C284	N	none	none	1	1	3C457	N	none	none	2	1
3C192	N	none	PJ	1	2	3C285	E	J	none	1	1						

Column [1]: 3CR catalogue source name. Column [2]: Spectral class. L: low excitation galaxies, Q: quasars, B and N: broad and narrow line radio galaxies respectively. Column [3] & [4]: Jet detections for north and south lobes respectively. J: definite jet, PJ: possible jet, CJ: counterjet, PCJ: possible counterjet.

Column [5] & [6]: Number of hotspots in the north and south lobe respectively. Columns [7] to [12] and columns [13] to [18] as for columns [1] to [6].

Table 5. The median fractional separation difference as defined by lobe size, $\langle x_{\text{lobe}} \rangle$, for each of the spectral class distributions

Spectral class	$\langle x_{\text{lobe}} \rangle$	Spectral class	$\langle x_{\text{lobe}} \rangle$
Q	0.185	NLRG, high $P_{178\text{MHz}}$	0.111
B	0.144	NLRG, low $P_{178\text{MHz}}$	0.092
Q and BLRG	0.184	NLRG	0.109
LERG	0.082	BLRG and low $P_{178\text{MHz}}$	0.101

4 CORES AND JETS

4.1 Observing effects

The effects of varying observing resolution should introduce little bias into the core measurements as they are bright features that are typically unresolved. For the jets, however, observing resolution will have an effect on detectability, which we now consider for the case of the total jet features.

30 per cent of sources in the sample have a definite jet, and a further 34 per cent have a possible jet; a summary of straight jet detections for the entire sample is given in Table 6, with the detection rate broken down by spectral class in Table 7. The total jet classifications are the same as for the straight jets but for the following three exceptions: the definite total jet is in the northern lobe in source 3C171 with a definite total counterjet detected in the southern lobe, a possible total counterjet is detected in the southern lobe of 3C20 and a definite total counterjet is detected in the southern lobe of 3C438.

The appearance of the jet features varies from source to source, and many of the detected jets do not cover the entire length from the core to the hotspot feature. Observing resolution and sensitivity should be an important factor in jet detectability; however,

the nature of any dependence on observational constraints is difficult to evaluate. The variation of observing resolution across the sample is potentially a source of observational bias, more so as this is accompanied by a variation in observing sensitivity.

To investigate the effect on total jet detectability, in Fig. 16 we plot the dynamic range (defined as the ratio of the maximum intensity to the off-source root mean square noise) against the effective observing resolution corresponding to the highest-resolution map for all the sample sources, binning by jet status. Sources lacking total jet features entirely are observed across the resolution and sensitivity range; thus there is no simple trend for those sources observed with relatively high resolution and high dynamic range to be associated with jet features.

Fig. 17 plots the fractional observed lobe length, f_l , against dynamic range, with data binned by total jet detection status. It might be expected that if the detected lobe emission in a source is more extensive (with f_l values closer to 1), it would be more difficult to detect a jet feature, but this does not seem to be the case. Definite and possible jet features are detected across the range in f_l . An additional aspect of jet detectability that can be considered is the jet location within the lobe. As mentioned previously, while in some sources a bright jet is observed to extend from the core to the lobe extremity, in many sources the jet is detected along a fraction of this length only. In Fig. 18, a histogram shows the distribution of the fractional jet position, f_{j_p} , for the definite and possible jets; 69 per cent of these objects have a jet that is traced from near the core, having $f_{j_p} < 0.1$. In order to examine the possibility that the jets are systematically becoming obscured as they progress through the lobe, the jet termination, f_{j_t} , is considered alongside f_{j_p} . f_{j_p} and

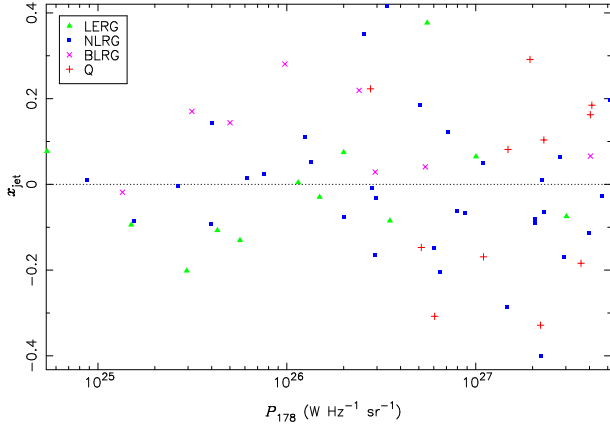


Figure 14. The fractional separation difference as defined by the straight jet side, x_{jet} , plotted against source luminosity at 178 MHz, P_{178} . The dotted line shows a fractional separation difference of zero.

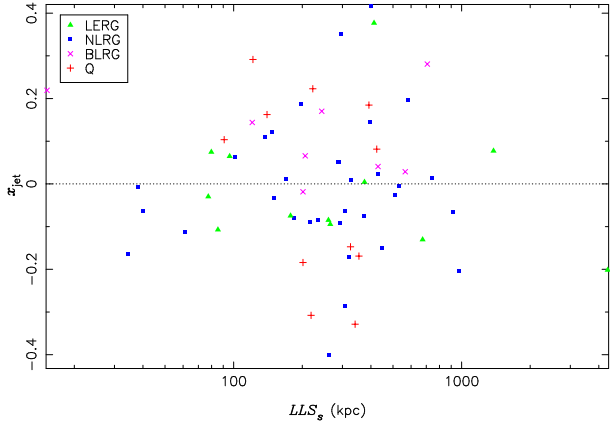


Figure 15. The fractional separation difference as defined by the straight jet side, x_{jet} , plotted against the largest linear source size, LLS_s . The dotted line shows a fractional separation difference of zero.

f_{ji} are plotted against the fractional lobe length, f_l , in Fig. 19. The dashed line represents f_{ji} , corresponding to a given f_l , that would be obtained if the observed total jet terminated on reaching the inner edge of the lobe. As there is no tendency for the f_{ji} data to crowd toward this line, jets are generally observed to extend into the lobe.

If the emitting material in the beam decelerated as it progresses from the core, and if the jet were detected more easily as this happens, then it might be expected that once the jet becomes detectable it could be traced to the hotspot region or the lobe extremity. This would be consistent with an anticorrelation between jet length and jet position. In Fig. 20 f_{ji} is plotted against f_{jp} and the dashed line shows the jet length corresponding to a given jet position that would indicate that the jet is observed continuously from its base to the lobe extremity. As there is no crowding toward this line, there is no strong tendency for this to be the case.

We conclude that, although the observing resolution should affect jet detectability, there is no obvious systematic bias in the sample that can be simply compensated for. The jet is not obviously less easily detected in sources with extensive lobes and the lack of jet detection does not appear to be a result of high lobe detectability.

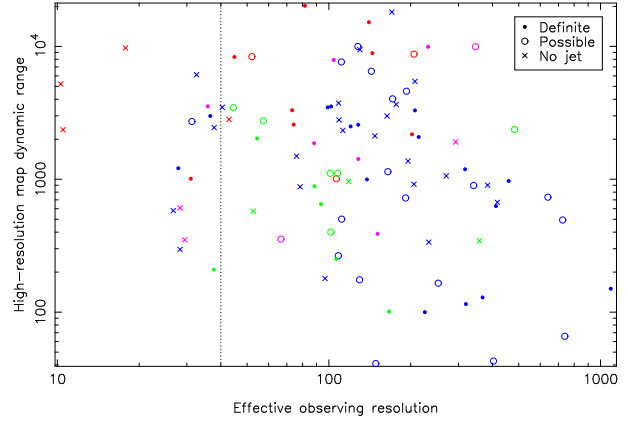


Figure 16. The dynamic range plotted against the high-resolution effective observing resolution, binned by total jet status. Filled circles: at least one definite jet detected, open circles: no definite jet detected but at least one possible jet, diagonal cross: no jet feature detected. Green: low excitation radio galaxies, blue: narrow line radio galaxies, magenta: broad line radio galaxies and red: quasars (on-line colour version). The dotted line shows a high-resolution effective observing resolution of 40.

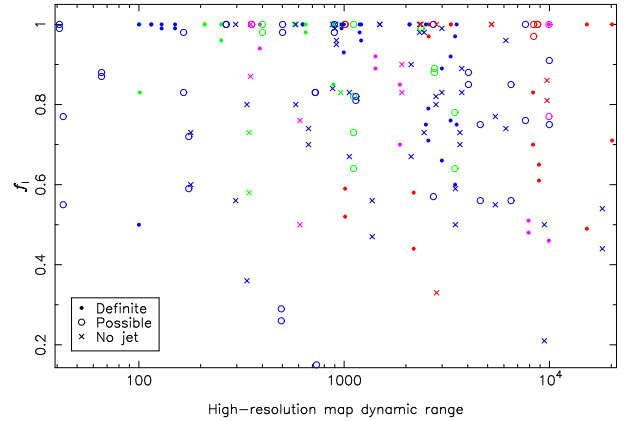


Figure 17. The fractional observed lobe length, f_{ji} , plotted against the dynamic range, binned by total jet status. Filled circles: at least one definite jet detected, open circles: no definite jet detected but at least one possible jet, diagonal cross: no jet feature detected. Green: low excitation radio galaxies, blue: narrow line radio galaxies, magenta: broad line radio galaxies and red: quasars (on-line colour version).

4.2 Trends with P_{178} , z and size

4.2.1 Cores

The core prominence distribution is plotted as a function of redshift in Fig. 21 and as a function of luminosity in Fig. 22. Any trend with redshift is weak but there is a tendency for the core prominence to decrease with increasing source luminosity and there is a lack of low-luminosity sources with faint cores. A Peto-Prentice test in which the sample objects (inclusive of all spectral classes) are divided by source luminosity at P_c shows that the trend for lower core prominence in higher-power sources is significant at the 99.5 per cent confidence level.

From Fig. 23 it can be seen that there is a tendency for smaller sources in general to be associated with lower core prominence. Binning the sample data by size, including all classes, a Peto-Prentice test between sources above and below $LLS_s = 200$ kpc shows no significant difference. (The 200-kpc size criterion was

Table 7. The jet detection data for the sample based on spectral class

Spectral class	jet features		definite jets		possible jets		null detection	
Q	73.3%	(11/15)	53.3%	(8/15)	20.0%	(3/15)	26.7%	(4/15)
B	72.7%	(8/11)	54.5%	(6/11)	18.2%	(2/11)	27.3%	(3/11)
N	59.6%	(34/57)	28.1%	(16/57)	31.6%	(18/57)	40.4%	(23/57)
E	80.0%	(12/15)	40.0%	(6/15)	40.0%	(6/15)	20.0%	(3/15)

chosen as evidence was found for morphological differences in lobe sizes above and below ~ 100 kpc; see Section 3.2.2.) However, if the sources are divided by spectral class, there is a significant tendency (at the 96.5 per cent confidence level) on a Peto-Prentice test for the smaller NLRGs to have lower core prominences: this was also noted by H98. It is not clear whether this is simply a result of the core-prominence/luminosity inverse correlation noted above in combination with the known luminosity/size inverse correlation, or whether (as suggested by H98) it is a genuine physical effect that is masked in other spectral types by beaming effects.

4.2.2 Jets

In Figs 24 and 25 the straight jet prominence is plotted against redshift and luminosity; there is no trend in the distribution with either parameter. A slightly broader range is found at $z \lesssim 0.3$; there is a marginally significant (93.7 per cent confidence level) difference between these low redshift sources and those with $z > 0.3$ on a K-S test. However, taking into account the upper limits in the data, a Peto-Prentice test does not suggest any significant difference in the distribution of p_j between the high and low luminosity sources, nor is any trend found with respect to redshift or source size. The many limits in the p_j data (around one third of the sample sources) may mask any trend.

4.3 Unification and beaming

4.3.1 Cores

The median core prominences for the different spectral classes are given in Table 8. The core prominence distribution of the Qs and BLRGs was compared with that of the NLRGs using a Peto-Prentice test. The difference in the distributions of Qs and high-luminosity NLRGs is significant above the 99.9 per cent confidence level, whilst that between the BLRGs and low power NLRGs is significant at the 97.4 per cent level. We find no significant difference between the p_c distributions of the LERGs and the BLRGs and low power NLRGs on a Peto-Prentice test.

In section 4.2.1 it was shown that there is evidence that the higher-power sources are associated with lower core prominence. Considering the spectral classes separately, Peto-Prentice tests show that the high-power BLRGs and NLRGs are significantly lower than the corresponding low-power BLRGs and NLRGs (note that there are only 2 sources in the high-power BLRG subsample), but there is no significant trend in the Qs or LERGs. The core prominence data are consistent with the idea that higher luminosity sources have higher Lorentz factors. The beaming factor is $\propto \gamma(1 - \beta \cos \theta)^{-2}$ (Scheuer & Readhead 1979, assuming the spectral index for the core features to be 0), and the range in this factor increases with γ . For a given γ , above a certain threshold angle of orientation with respect to the observer's line-of-sight, θ_1 , the emission will be Doppler suppressed and the observed core prominence will be lower than the intrinsic value. As γ increases, θ_1 decreases and the suppression of parsec scale jet emission at

Table 8. The median core prominence, $\langle p_c \rangle$, for the different spectral classes.

Spectral class	$\langle p_c \rangle / 10^{-3}$	Spectral class	$\langle p_c \rangle / 10^{-3}$
Q	2.030	NLRG, high $P_{178\text{MHz}}$	0.086
B	0.915	NLRG, low $P_{178\text{MHz}}$	0.335
Q and BLRG	1.061	NLRG	0.134
LERG	0.592	BLRG and low $P_{178\text{MHz}}$	0.524

large θ becomes strong. In Qs, VLBI observations have reported $\gamma \sim 5-10$ for some sources (e.g., Zensus 1997; Hough et al. 2002). This would result in Doppler-boosted cores in broad-line objects and Doppler-suppressed cores for the equivalent NLRGs, assuming $\theta_c \approx 40 - 50^\circ$. If sources of lower luminosity were associated with lower γ , the core prominence of BLRG sources would not be as strongly boosted as the Qs (though there is no significant difference between the core prominence of Qs and BLRGs) and also the Doppler suppression of the NLRG cores would be less strong. This latter point could lead to generally lower core prominence being found in *higher*-luminosity NLRGs.

4.3.2 Jets

The one-sidedness of FR II jets is difficult to account for without beaming. There are very few counterjets detected in the sample but the general symmetry of the extended structure requires there to be bi-polar beams emanating from the central engine. The fact that so few counterjets are detected at all suggests that kiloparsec scale jet emission is beamed.

The straight jet detection statistics indicate a difference with spectral class that is consistent with beaming models (see Table 7, previously discussed in section 4.1). The Qs and BLRG sources have a similarly high jet-feature detection rate (~ 73 per cent), with definite jets detected in ~ 53 per cent of the sources. (The Q sources with no jet detected are observed at relatively low resolution, $\lesssim 40$ beams across the source in the high-resolution map; this is not true for the BLRGs). For the NLRG class, jet features are found in 60 per cent of sources, with only 28 per cent of NLRGs having a definite jet detected. The upper limits of the NLRG and LERG sources are distributed across the range in observing resolution.

The median straight jet prominence *for detected jets only* for each of the spectral classes is shown in Table 10. When we compare the straight jet prominences of the broad-line objects (Q and BLRG) to the NLRG with a Peto-Prentice test, taking upper limits into account, we find a difference that is significant at the 99.6 per cent confidence limit in the sense that the median prominence of the broad-line objects is significantly higher. This confirms the earlier result of H98. The difference in jet prominence is still significant if the sample is divided into low-luminosity and high-luminosity sub-samples, at the 98.7 per cent and 94.4 per cent confidence levels respectively – the marginal significance in the high-luminosity bin presumably arises from the large fraction of upper limits in the NLRG in this sample. There is no significant difference between the LERG and other (NLRG/BLRG/Q) straight jet prominence dis-

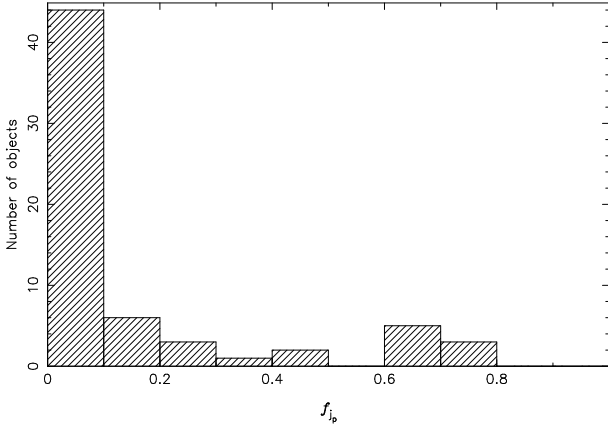


Figure 18. Histogram of the fractional jet position, f_{jp} , for the sample.

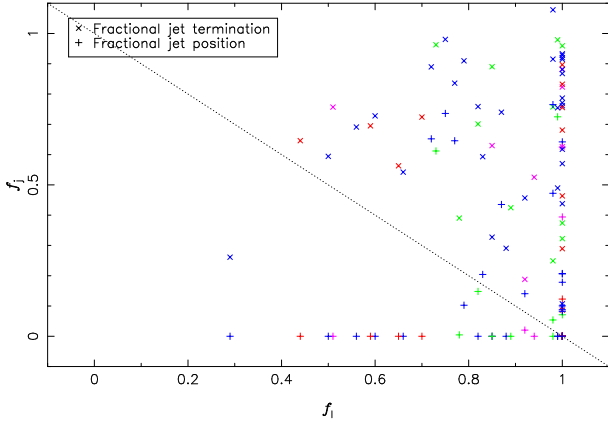


Figure 19. The fractional jet position, f_{jp} , and fractional jet termination, f_{jt} , plotted against the fractional observed lobe length, f_l , of the corresponding lobe. Green: low excitation radio galaxies, blue: narrow line radio galaxies, magenta: broad line radio galaxies and red: quasars (on-line colour version). The dotted line is the line of $f_{jt} = 1 - f_{jp}$.

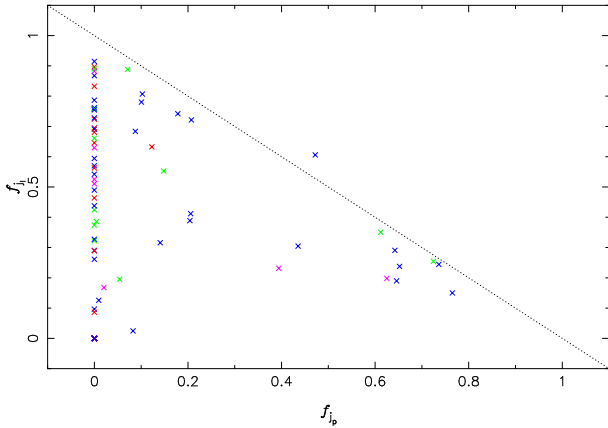


Figure 20. The fractional jet length, f_{jl} , plotted against the fractional jet position, f_{jp} , of the corresponding lobe. Green: low excitation radio galaxies, blue: narrow line radio galaxies, magenta: broad line radio galaxies and red: quasars (on-line colour version). The dotted line is the line of $f_{jl} = 1 - f_{jp}$.

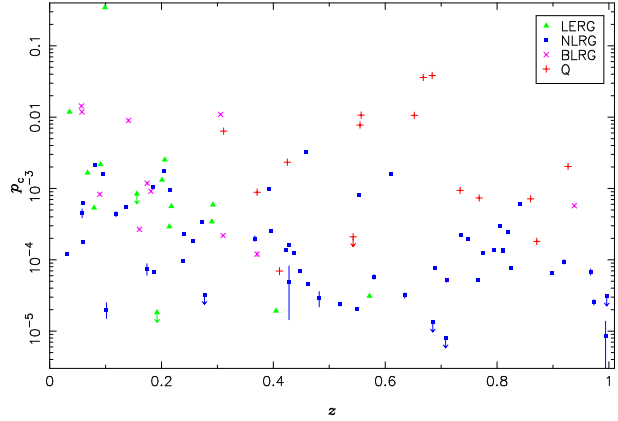


Figure 21. The core prominence, p_c , plotted against redshift, z . Vertical bars indicate errors, arrows indicate upper limits.

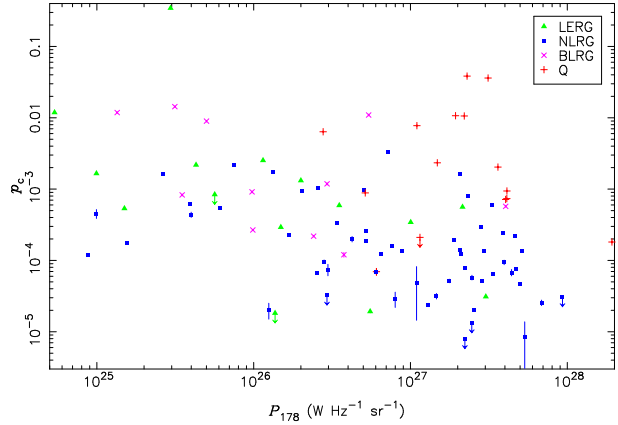


Figure 22. The core prominence, p_c , plotted against the source luminosity at 178 MHz, P_{178} . Vertical bars indicate errors, arrows indicate upper limits.

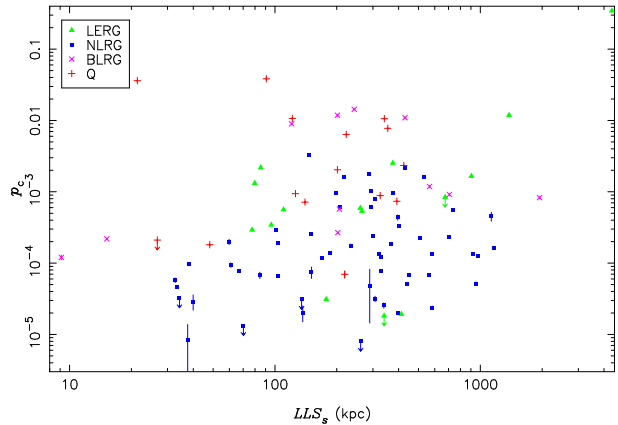


Figure 23. The core prominence, p_c , plotted against the largest linear source size, LLS_g . Vertical bars indicate errors, arrows indicate upper limits.

tributions. These differences in prominence are consistent with the expectations from unified models and beaming.

In addition, the Laing-Garrington effect (as discussed in section 1), in which the jet occurs in the lobe that shows less depolarization, can be considered. Depolarization data were available in the literature (Table 9) for 60 of the sample sources, 41 of which have detected jets (possible and definite). Of these 41 sources, 30 have the jet on the less depolarized side (73 per cent). On a bino-

Table 9. Depolarisation data taken from the literature for our sample

Source	Jet side	Depolarization		λ		Reference	Source	Jet side	Depolarization		λ		Reference
		N lobe	S lobe	high [GHz]	low [GHz]				N lobe	S lobe	high [GHz]	low [GHz]	
4C12.03	N	-	-	-	-	-	3C236	N	-	-	-	-	-
3C6.1	-	0.50	0.27	8.1	2.7	1	4C74.16	S	0.23	-0.01	5.0	1.5	6
3C16	N	-0.38	-0.28	4.8	1.4	2	3C244.1	N	0.27	0.30	8.1	1.4	1
3C19	S	-	-	-	-	-	3C247	-	0.84	0.00	5.0	1.5	12
3C20	N	0.50	0.67	8.1	1.4	1	3C249.1	N	0.27	0.37	5.0	1.5	10
3C22	N	-0.05	0.54	5.0	1.5	3	3C254	-	0.27	0.68	5.0	1.5	12
3C33	S	-	-	-	-	-	3C263	S	-	-	-	-	-
3C33.1	S	0.05	0.04	4.8	1.5	4	3C263.1	-	0.91	0.56	5.0	1.5	12
3C34	N	0.21	0.38	4.8	1.5	5	3C265	N	-0.26	-0.19	4.8	1.4	2
3C35	-	-	-	-	-	-	3C268.1	-	-0.27	0.19	4.8	1.4	2
3C41	S	0.06	0.02	5.0	1.5	6	3C268.3	-	-	-	-	-	-
3C42	-	-0.01	0.00	4.8	1.4	2	3C274.1	S	0.11	0.08	2.4	1.0	9
3C46	S	-0.12	-0.07	4.8	1.4	2	3C275.1	N	0.05	0.42	5.0	1.5	6
3C47	S	0.82	0.05	4.9	1.5	7	3C277.2	S	-0.09	0.54	5.0	1.5	11
3C55	S	0.11	0.00	5.0	1.5	3	3C280	-	-0.21	-0.29	4.8	1.4	2
3C61.1	-	0.58	0.54	4.8	1.5	4	3C284	-	0.04	0.31	2.4	1.0	9
3C67	N	0.35	-0.65	4.9	1.6	8	3C285	N	-	-	-	-	-
3C79	-	0.44	0.05	2.4	1.0	9	3C289	-	0.87	0.66	5.0	1.5	12
3C98	N	-	-	-	-	-	3C292	-	-	-	-	-	-
3C109	S	0.53	0.52	4.8	1.5	4	3C295	-	-	-	-	-	-
4C14.11	N	-	-	-	-	-	3C299	-	-0.30	-0.09	4.8	1.4	2
3C123	-	-	-	-	-	-	3C300	N	0.11	0.77	2.4	1.0	9
3C132	S	0.31	0.14	2.4	1.5	9	3C303	N	-	-	-	-	-
3C153	S	-	-	-	-	-	3C319	-	-	-	-	-	-
3C171	S	0.14	0.40	8.1	2.7	1	3C321	N	-	-	-	-	-
3C172	-	0.26	0.27	2.4	1.0	9	3C325	N	-	-	-	-	-
3C173.1	N	-	-	-	-	-	3C326	-	-	-	-	-	-
3C175	S	1.00	1.00	5.0	1.5	10	3C330	-	0.09	0.29	5.0	1.5	13
3C175.1	S	0.11	0.54	5.0	1.5	11	3C334	S	0.23	0.09	5.0	1.5	6
3C184	-	-	-	-	-	-	3C336	S	1.00	0.74	2.4	1.0	10
3C184.1	N	-	-	-	-	-	3C341	S	-0.18	-0.21	4.8	1.4	2
DA240	S	-	-	-	-	-	3C337	S	0.16	0.47	5.0	1.5	11
3C192	S	0.58	0.82	2.4	1.0	9	3C340	-	0.21	0.03	4.8	1.5	5
3C196	-	-	-	-	-	-	3C349	-	-	-	-	-	-
3C200	S	0.39	0.08	5.0	1.5	6	3C351	N	0.46	-0.44	4.8	1.4	2
4C14.27	N	-0.17	-0.01	4.8	1.4	2	3C352	N	0.28	0.74	5.0	1.5	6
3C207	S	0.60	0.16	5.0	1.5	6	3C381	-	0.06	0.04	4.8	1.5	4
3C215	S	0.45	0.21	5.0	1.5	6	3C382	N	0.09	0.16	2.5	1.5	10
3C217	-	0.20	0.67	5.0	1.5	11	3C388	S	-	-	-	-	-
3C216	-	-	-	-	-	-	3C390.3	N	0.01	0.03	1.5	0.3	10
3C219	S	0.53	0.55	4.8	1.5	4	3C401	S	-	-	-	-	-
3C220.1	N	-	-	-	-	-	3C427.1	N	-	-	-	-	-
3C220.3	-	-	-	-	-	-	3C433	N	-	-	-	-	-
3C223	N	0.07	0.11	2.4	1.0	9	3C436	S	-	-	-	-	-
3C225B	-	-	-	-	-	-	3C438	N	-	-	-	-	-
3C226	-	-	-	-	-	-	3C441	N	0.28	0.06	5.0	1.5	6
4C73.08	-	-	-	-	-	-	3C452	S	-	-	-	-	-
3C228	S	0.30	0.05	4.8	1.5	5	3C455	-	-0.45	0.03	4.9	1.6	8
3C234	N	0.55	0.56	4.8	1.5	4	3C457	-	0.00	-0.09	4.8	1.4	2

Column [1]: 3CR catalogue source name. Column [2]: jet side. Column [3] & [4]: depolarization measure, DPM , for north and south lobe respectively, where $DPM = (m_h - m_l)/(m_h + m_l)$, m_h and m_l being the fractional polarization measured at the higher and lower frequency respectively. Column [5] & [6]: Frequency of high and low frequency maps respectively. Column [7]: References for data. (1): Wright (1979), (2): Goodlet et al. (2004), (3): Fernini et al. (1993), (4): Dennett-Thorpe, Barthel & van Bemmel (2000), (5): Johnson, Leahy & Garrington (1995), (6): Garrington, Conway & Leahy (1991), (7): Fernini et al. (1991), (8): Akujor & Garrington (1995), (9): Conway et al. (1983), (10): Garrington & Conway (1991), (11): Pedelty et al. (1989), (12): Liu & Pooley (1991), (13): Fernini (2001). Columns [8] to [14] and [15] to [21] as for [1] to [7].

mial test this is a significant trend at the 99.8 per cent confidence limit. The effect would be expected to be stronger for broad line sources and there were depolarization data available for 16 of the 26 Qs and BLRGs: 75 per cent of these showed correlation between the jet-side lobe and the less depolarized lobe (marginally significant at the 96 per cent level on a binomial test). Given that other properties of the sources and their environments are known to affect source depolarization, and that our data are necessarily heterogeneous, these results also seem to be in good agreement with the expectation from beaming models.

4.3.3 Correlation between core and straight jet prominence

Considering all the data, including upper limits, the correlation between jet prominence and core prominence is significant, at the 99.9 per cent confidence level, on a modified Kendall's τ test as implemented in ASURV. This result is consistent with the correlation found by H98 in a sample with substantially fewer upper limits.

In Figs 26 and 27 we plot the core prominence data against source luminosity for both the entire sample and the NLRG class respectively, binning the data according to the straight jet detection status indicated as before. For the sample as a whole (Fig. 26) those sources with at least one jet detection have higher core prominence. As Qs and BLRGs are generally observed to have brighter jets this is to be expected and is further illustrated in Fig. 28. However, even when considering the NLRG population separately (Fig. 27) it is clear that the NLRGs with definite jet detections are also associated with relatively higher core prominence. A Peto-Prentice test applied to the core prominence data between all sources with at least one definite or possible straight jet and those with no detection indicates the jetted sources have higher core prominence, significant at the 99.9 per cent confidence level.

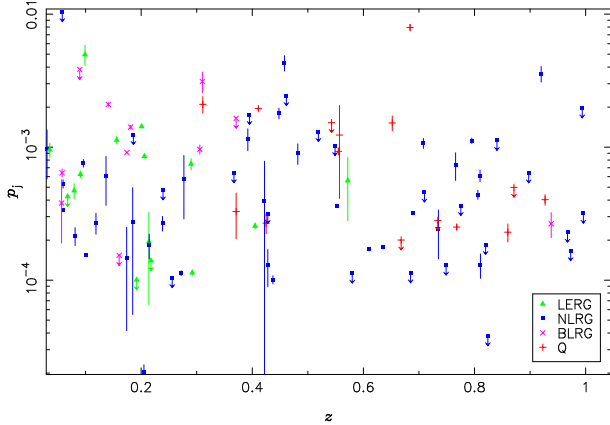


Figure 24. The straight jet prominence, p_j , plotted against z . Vertical bars indicate errors, arrows indicate upper limits.

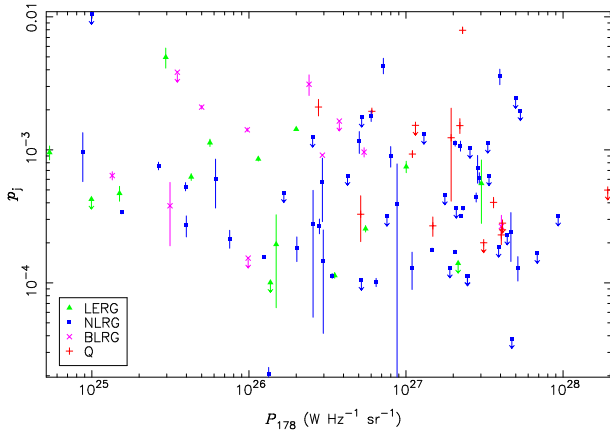


Figure 25. The straight jet prominence, p_j , plotted against the source luminosity at 178 MHz, P_{178} . Vertical bars indicate errors, arrows indicate upper limits.

Table 10. The median straight jet prominence for detected jets only, $\langle p_j \rangle$, for each of the spectral class distributions.

Spectral class	$\langle p_j \rangle / 10^{-3}$	Spectral class	$\langle p_j \rangle / 10^{-3}$
Q	0.930	NLRG, high $P_{178\text{MHz}}$	0.134
B	0.936	NLRG, low $P_{178\text{MHz}}$	0.440
Q and BLRG	0.930	NLRG	0.351
LERG	0.690	BLRG and low $P_{178\text{MHz}}$	0.619

5 HOTSPOTS

5.1 Hotspot prominence and size

5.1.1 Observing effects

A summary of hotspot detections in the sample (as defined by the hotspot criteria in section 2.2.6) is given in Table 6. From this table it can be seen that 58 per cent of sources have one hotspot per lobe and 34 per cent have at least one lobe with more than one hotspot feature. Only 9 sources have one lobe that lacks a hotspot, and only 1 source of the 98 lacks hotspots entirely. Observations of sources with a single bright, compact hotspot had led to the suggestion that hotspots corresponded to enhanced emission associated with the beam termination shock, but as multiple features are often detected at high resolution, this interpretation is too simplistic. However, it is still thought that the hotspots correspond to shocks at or near the

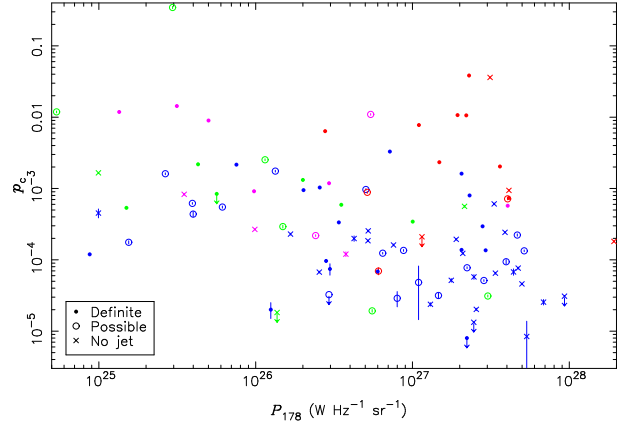


Figure 26. The core prominence, p_c , for the entire sample plotted against the source luminosity at 178 MHz, P_{178} , binned by straight jet detection status. Filled circles: at least one definite jet detected, open circles: no definite jet detected but at least one possible jet, diagonal cross: no jet feature detected. Vertical bars indicate errors, arrows indicate upper limits. Green: low excitation radio galaxies, blue: narrow line radio galaxies, magenta: broad line radio galaxies and red: quasars (on-line colour version).

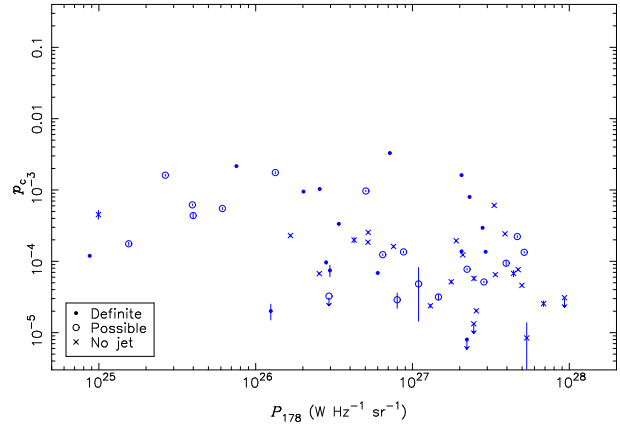


Figure 27. The core prominence, p_c , for the NLRGs plotted against the source luminosity at 178 MHz, P_{178} , binned by straight jet detection status. Filled circles: at least one definite jet detected, open circles: no definite jet detected but at least one possible jet, diagonal cross: no jet feature detected. Vertical bars indicate errors, arrows indicate upper limits. Green: low excitation radio galaxies, blue: narrow line radio galaxies, magenta: broad line radio galaxies and red: quasars (on-line colour version).

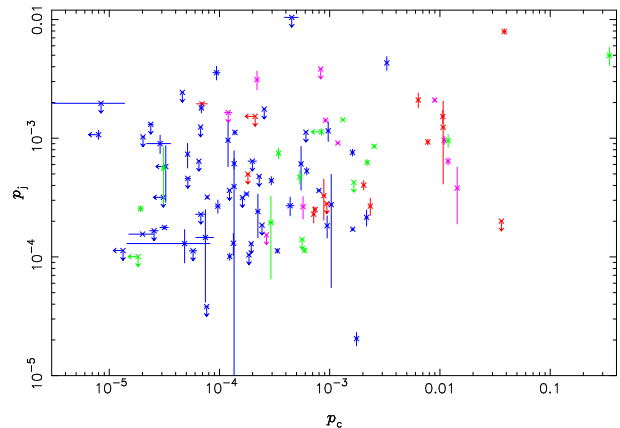


Figure 28. Jet prominence of definite and possible straight jets, p_j , plotted against core prominence, p_c , for all spectral classes. Vertical bars indicate errors, arrows indicate upper limits. Green: low excitation radio galaxies, blue: narrow line radio galaxies, magenta: broad line radio galaxies and red: quasars (on-line colour version).

beam termination, although the exact relation between the observed emission and the physical structure is not understood.

From the sample sources mapped at more than one resolution, it can be seen that hotspot features generally appear more diffuse at the lower resolution, with a larger size fitted by JMFIT. This effect of observing resolution on apparent hotspot size can be quantitatively considered by making use of the fractional hotspot size, f_h , defined in section 2.2.6. In Fig. 29 we plot f_h against the effective observing resolution for all sources in the sample; from this figure it can be seen that relatively smaller hotspots are indeed associated with sources observed at relatively higher resolution.

The larger the region that is identified as the hotspot (that is, the higher f_h is) the greater the hotspot prominence may potentially be, as more flux is included in the hotspot flux measurement. If low observing resolution results in larger hotspots, this may cause a bias for more prominent hotspots, if more lobe emission is included in the hotspot measurement. Fig. 30 plots hotspot prominence against f_h , and it can be seen that sources with larger f_h correspond with higher prominence; very approximately $p_h \propto f_h^2$, though for $f_h < 0.1$ there is little correlation between the two quantities.

We conclude that hotspot properties are strongly affected by observing resolution and that this is difficult to compensate for. This should be borne in mind when considering the following results.

5.1.2 Trends with P_{178} , z and size

No apparent trends in the sample can be seen in the plots of hotspot prominence, binned by high-resolution effective observing resolution, against z , P_{178} and LLS_s in Figs 31 to 33 respectively. Various authors, including H98 and Kharb et al. (2008), have found a significant correlation between lobe linear size and hotspot size, which is also apparent in our data (Fig. 34). The correlation seen here as determined by Kendall's τ coefficient is significant above the 99.9 per cent confidence limit.

However, it can be noted that there are serious potential biases in the hotspot-size lobe-size correlation result, given that the observing resolution used is also strongly correlated with source angular size. One way of circumventing this is to compare hotspot data from a single map. In Fig. 35 we plot the *fractional* sizes (f_h) of the primary hotspot in each lobe against each other. If the two fractional hotspot sizes were uncorrelated, this would suggest that there is no tendency for the hotspots to 'know about' the linear size of the source, while a strong correlation would be consistent with the notion that the hotspot size is proportional to lobe size and support the hypothesis of self-similarity in the lobe. We find that the Kendall's τ test shows a correlation significant above the 99.9 per cent confidence level. Thus there is some support in the data for a real physical correlation between hotspot and lobe size. We also note that the hotspot size-linear size correlation is still highly significant if we consider only the subsample of objects (approximately half of the total) that are observed with more than 100 restoring beams across the source. A correlation between hotspot and lobe size supports models of self-similarity in which the beam's working surface maintains pressure balance as it extends (Carvalho & O'Dea, 2002).

In section 3.2.2 we suggested that there was some evidence that the R_{ax} distribution is consistent with self-similar source expansion on smaller scales. Considering the sample by binning with respect to size, using a cutoff of $LLS_s = 200$ kpc as before, there is a difference in the f_h distributions of the small and large sources significant above the 99.9 per cent confidence level on a K-S test.

Binning using luminosity (with cutoff P_c) gives evidence of a difference in the high and low power sources also as a K-S test suggests that they are different at the 93 per cent confidence level. The difference appears to be in the sense that the more powerful/smaller sources have a broader distribution of hotspot fractional size. This may well simply be an observational effect: many of the sources with the largest fractional hotspot size are a) small, b) powerful and c) observed at low effective resolution. We cannot draw strong conclusions about self-similarity from these results.

5.1.3 Beaming and unification

If beaming affects the observed hotspot prominence then the brighter hotspot might be expected to be correlated with the straight jet side. The most compact feature may also show such a correlation, if the approaching and receding hotspot emission corresponds to a different physical region within the flow. Laing (1989) suggested such a model, whereby the approaching hotspot emission originated in a region of higher β flow, closer to the core of the beam. The model predicted that the most compact hotspot would be correlated with the jet side.

In our analysis we consider the ratio of f_h in each lobe rather than the hotspot size alone and both this ratio and the corresponding flux ratio are defined by taking the ratio of the straight jet-side measurement to that of the counterjet. The hotspot size ratio will therefore be less than one if the most relatively compact hotspot is on the jet side and the hotspot flux ratio will be more than one if the more prominent hotspot is on the jet side. The hotspot flux and f_h ratios as defined by jet side are plotted against source size in Fig. 36 and 37. As not all sources have a straight jet detection this introduces a bias when we consider the data quantitatively and this should be borne in mind.

We find that there are no significant tendencies for brighter hotspots to be found on the jet side, for any spectral class. However, the f_h data suggest that the more relatively compact hotspot is correlated with the jet side in quasars: 10/11 jetted Qs have the more compact hotspot on the jet side, a result significant at the 99.4 per cent level on a binomial test.

5.2 Hotspot recession

5.2.1 Observing resolution

The effect of observing resolution on the measured hotspot recession has been addressed by the application of a resolution-correction factor (G99) as discussed in section 2.2.1. This correction factor should ensure that the hotspot recession parameter η will be 1 for hotspots located at the lobe extremity.

5.2.2 Trends with P_{178} , z and size

ζ , the source hotspot recession parameter (defined in section 2.2.7), is plotted against redshift, source luminosity and size in Figs 38 to 40 respectively. There is no significant tendency for higher-luminosity sources to be more recessed, but a K-S test binning the sample using a divide of 200 kpc does indicate that smaller sources are more recessed with significance at the 99.7 per cent confidence level.

5.2.3 Unification

For sources not lying close to the plane of the sky geometric effects may cause a hotspot that is intrinsically positioned near the lobe edge to appear set back in the lobe. Thus orientation effects may contribute to the observed range in ζ . Gilbert (2001) considered hotspot recession for the sub-sample of sources with $z \leq 0.5$. Sources were modelled as an expanding ellipse with a Gaussian emission density, which was rotated with respect to the observer's line-of-sight. Taking different expansion speeds (into the relativistic regime) and different orientations the model was compared to the data by predicting number counts for recessed sources. Gilbert concluded that effects other than simple geometric effects contributed to the observed recession distribution. Around 15 per cent of sources were expected to have $\zeta < 0.9$ from the model when in fact 26 per cent of his sample were observed to have this degree of recession. Furthermore, only around 3 per cent of sources were predicted to show strong recession, with $\zeta < 0.8$, whereas close to 13 per cent does. When we consider our current sample, 32 per cent of sources (including all spectral classes) have $\zeta < 0.9$ while 10 per cent have $\zeta < 0.8$. The conclusion that effects other than simple geometric effects from source orientation contribute to the observed hotspot recession is thus valid for our sample too.

A W-M-W test comparing the Qs and high-luminosity NLRGs shows that the difference in median ζ between the spectral classes is not significant, although a K-S test shows a difference in the distributions for the samples at the 94.5 per cent level, consistent with the observed broader spread of the Qs (Figs 38 to 40) but formally not significant. There are no significant differences between the low luminosity spectral classes and there is no significant tendency for the straight jet side to be any more or less recessed than that of the counterjet.

6 DISCUSSION

6.1 Summary of results

Table 11 contains a summary of all statistical results from the preceding sections. The consequences of these for physical models of FRII sources are discussed in the following sections.

6.2 Jets and evidence for beaming on kiloparsec scales

On kiloparsec scales, jets have been detected in 30 per cent of sources, with a further 34 per cent having a feature that is classified as a possible jet. While observing resolution and sensitivity are clearly factors in jet detectability, we found that jets are more commonly detected in Qs and BLRGs, with more definite jets associated with these classes than for the NLRGs of any luminosity. This is consistent with the expectations from unification and beaming models. Statistical tests taking into account the large number of upper limits on jet prominence show that the broad-line and narrow-line objects have jet prominences that differ in the sense expected from beaming if the broad-line objects make smaller angles to the line of sight.

Further evidence in support of beaming in the kpc-scale jets is the correlation between core and jet prominence; we showed that there are significantly more prominent cores in those sources with a detected kpc-scale jet feature, while core prominence and jet prominence are correlated in our data even in the presence of upper limits. Since we know beaming is important in the cores from VLBI observations of apparent superluminal motion (e.g., Zensus

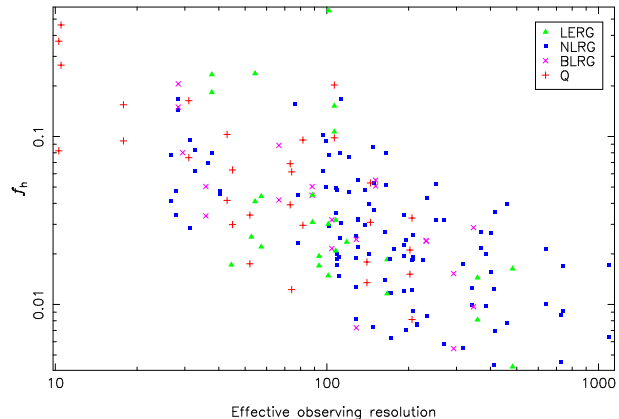


Figure 29. The fractional hotspot size, f_h , plotted against the corresponding high-resolution effective observing resolution.

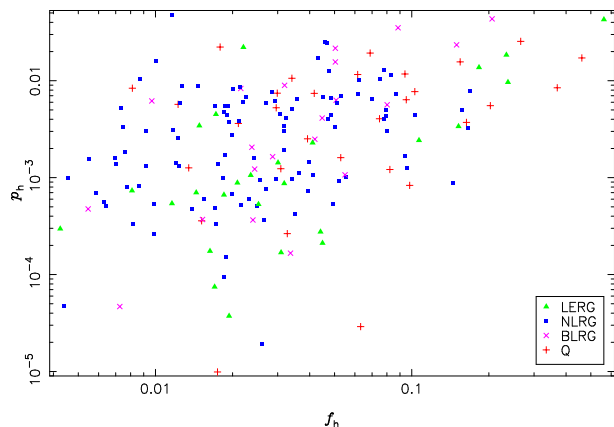


Figure 30. The hotspot prominence, p_h plotted against the fractional hotspot size, f_h .

1997; Hough et al. 2002), these results require beaming to be important in the kiloparsec-scale jets as well. In addition, we found that the Laing-Garrington effect, in which the less depolarized lobe is correlated with the approaching (jet-side) lobe, is detected in the sample for all jetted sources for which depolarization data were available. This was the case for 41 sources, 30 of which had the jet side corresponding to the less depolarized lobe, significant on a binomial test at the 99.8 per cent confidence level.

Thus the data strongly support the idea that the jets remain relativistic on kpc scales. We will explore the implications of our measurements for bulk speeds in the jets and cores in a future paper.

Some evidence was found for beaming effects in the hotspot data, in that there was a tendency for the most compact hotspot to be on the same side as the jet feature in quasars (parametrizing hotspot compactness by the fractional hotspot size), consistent with the results of Bridle et al. (1994). However, no corresponding correlation between the jet side and the brighter hotspot was found in any emission-line class, which is inconsistent with the results of Laing (1989). The data thus provide only limited support to the idea that relativistic beaming plays an important role in the appearance of hotspots: most likely the varied appearance of these features is dominated by the local conditions, with beaming playing a secondary role.

Table 11. Summary of statistical tests.

Proposition	Conclusion	Details	Section
Are high power sources statistically smaller?	No	W-M-W test compared high and low luminosity sources using a cutoff of $5 \cdot 10^{26} \text{ W Hz}^{-1} \text{ sr}^{-1}$, including all sources. Null hypothesis only rejected at 86 per cent confidence level.	section 3.1.2
Are Qs and BLRGs statistically smaller than NLRGs of equivalent luminosity?	No	W-M-W test compared Qs with high power NLRGs, and BLRGs with low power NLRGs. Although medians of Qs and BLRGs lower, difference not significant. Null hypothesis only rejected at 70 and 35 per cent confidence level.	section 3.1.3
Are LERGs statistically smaller than BLRGs and low power NLRGs	No	W-M-W test compared LERGs with BLRGs and low power NLRGs. Null hypothesis only rejected at 12 per cent confidence level.	section 3.1.3
Are lobes broader in sources observed at low resolution?	Yes	W-M-W test compared sources observed with 40 or fewer restoring beams across LLS_s with those observed at higher resolution. Significant above 99.9 per cent confidence level.	section 3.2.1
Is there a systematic tendency towards lower R_{ax} in sources observed at relatively low resolution?	Yes	W-M-W test compared sources observed with 40 or fewer restoring beams across LLS_s with those observed at higher resolution. Significant above the 99.9 per cent confidence level	section 3.2.1
Is there a significant difference in the R_{ax} distribution across the power and redshift range?	No	K-S test between sources binned by P_{178} using a cutoff of $5 \cdot 10^{26} \text{ W Hz}^{-1} \text{ sr}^{-1}$, and binned by z using a cutoff of 0.5, including all sources. Null hypothesis only rejected at 4 and 22 per cent confidence levels respectively.	section 3.2.2
Is there a significant tendency towards lower R_{ax} in smaller sources?	Yes	W-M-W test compared small and large sources using a cutoff of 100 kpc, including all sources. Significant above 99.9 per cent confidence level.	section 3.2.2
Is there a significant tendency towards lower R_{ax} in Qs than in NLRGs?	Yes	W-M-W test compared Qs with high power NLRGs. Significant at the 99.6 per cent confidence level.	section 3.2.3
Is there a significant tendency towards lower R_{ax} in BLRGs than in NLRGs?	No	W-M-W test compared BLRGs with low power NLRGs. Null hypothesis only rejected at 86 per cent confidence level.	section 3.2.3
Is there a significant tendency towards lower w in Qs than in high-power NLRGs	No	W-M-W test compared Qs with high-power NLRGs. Null hypothesis only rejected at 48 per cent confidence level.	section 3.2.3
Is there a significant difference in the R_{ax} distribution of LERGs compared to BLRGs and NLRGs?	No	K-S test compared LERG distribution with that of combined BLRGs and low power NLRGs. Null hypothesis only rejected at 64 per cent confidence level.	section 3.2.3
Is there a significant difference in the x_{lobe} distribution across the power and size range?	No	K-S test between sources binned by P_{178} using a cutoff of $5 \cdot 10^{26} \text{ W Hz}^{-1} \text{ sr}^{-1}$, and binned by LLS_s using a cutoff of 200 kpc, including all sources. Null hypothesis only rejected at 41 and 73 per cent confidence level respectively.	section 3.3.1
Is there a significant tendency towards higher x_{lobe} in Qs than in NLRGs?	Yes	W-M-W test compared Qs with high power NLRGs. Significant at the 99.7 per cent confidence level.	section 3.3.2
Is there a significant tendency for x_{lobe} to be higher in BLRGs than in NLRGs?	No	W-M-W test compared BLRGs with low power NLRGs. Null hypothesis only rejected at 55 per cent confidence level.	section 3.3.2
Is there a significant difference in the x_{lobe} distribution of LERGs compared to BLRGs and NLRGs?	No	K-S test compared LERG distribution with that of combined BLRGs and low power NLRGs. Null hypothesis only rejected at 83 per cent confidence level.	section 3.3.2

Table 11 continued.

Proposition	Conclusion	Details	Section
Is there a significant tendency for x_{jet} to be positive in BLRGs?	Yes	Binomial test shows tendency for BLRGs to have positive x_{jet} values; significant at the 96.5 per cent confidence level.	section 3.3.2
Is there a significant tendency for x_{jet} to be positive in Qs, NLRGs and LERGs?	No	Binomial test shows no significant tendency for Qs, NLRGs or LERGs to have positive x_{jet} values; null hypothesis only rejected at the 50, 20 and 19 per cent confidence level respectively.	section 3.3.2
Is there a significant tendency for x_{jet} to be positive in smaller sources?	No	Binomial test suggests no significant tendency for small sources to have positive x_{jet} values; null hypothesis only rejected at 81 per cent confidence level.	section 3.3.2
Is there a significant difference in the x_{jet} distribution across size range?	No	K-S test between sources binned by LLS_s using a cutoff of 200 kpc, including all sources. Null hypothesis only rejected at 77 per cent confidence level.	section 3.3.2
Is there a significant tendency toward lower p_c in higher-power sources?	Yes	Peto-Prentice test compared high and low power sources using a cutoff of $5 \cdot 10^{26} \text{ W Hz}^{-1} \text{ sr}^{-1}$, including all sources. Significant at 99.5 per cent confidence level.	section 4.2.1
Is there a significant tendency toward lower p_c in smaller sources?	No	Peto-Prentice test compared large and small sources using a cutoff of $LLS_s = 200$ kpc, including all sources. Null hypothesis only rejected at 85 per cent confidence level.	section 4.2.1
Is there a significant tendency toward lower p_c in smaller NLRGs?	Yes	Peto-Prentice test compared large and small NLRG using a cutoff of $LLS_s = 200$ kpc. Null hypothesis rejected at 96.5 per cent confidence level.	section 4.2.1
Is there a significant tendency for the p_j distribution to vary across the power, redshift and size range?	No	Peto-Prentice test compared high and low-power sources dividing at $L = 5 \times 10^{26} \text{ W Hz}^{-1} \text{ sr}^{-1}$, at $z = 0.5$ and at $LLS_s = 200$ kpc including all sources. Null hypotheses only rejected at 77, 19 and 34 per cent confidence levels respectively.	section 4.2.2
Is there a significant tendency toward higher p_c in Qs than in NLRGs?	Yes	Peto-Prentice test compared Qs and low power NLRGs. Significant above 99.9 per cent confidence level.	section 4.3.1
Is there a significant tendency toward higher p_c in BLRGs than in NLRGs?	Yes	Peto-Prentice test compared BLRGs and low power NLRGs. Significant at 97.4 per cent confidence level.	section 4.3.1
Is there a significant tendency for the LERGs p_c distribution to differ?	No	Peto-Prentice test compared LERGs and BLRGs and low power NLRGs. Null hypothesis only rejected at 34 per cent confidence level.	section 4.3.1

6.3 Source morphology

A significant trend in R_{ax} with source size is found across the sample (Section 3.2.2). The observed range in R_{ax} is much greater for sources larger than ≈ 200 kpc. While observational effects were found to be a source of bias in the R_{ax} data, with lower R_{ax} values in sources observed at lower resolution, we concluded that the trend with source size does not result from such a bias but represents a real physical trend.

Early work on source expansion models assumed that the cocoon would remain overpressured as the source evolved, which would result in self-similar expansion (e.g., Begelman & Cioffi, 1989), but subsequently it was demonstrated that this would only be the case for sources in an ambient medium with a decreasing density profile (e.g., Falle 1991; Kaiser & Alexander 1997). However, numerical simulation has showed that the lateral expansion of the source will slow as the cocoon comes into pressure balance with the ambient medium and that this will occur in a typical source before it has grown to any considerable size (e.g., Carvalho & O’Dea 2002), a result consistent with the known X-ray properties of the environments of FRIIs (e.g. Hardcastle & Worrall 2000). The R_{ax} data are consistent with the idea that radio sources in general go through an early self-similar expansion phase where R_{ax} is approx-

imately constant on size scales of the order of the size of the host galaxy, after which lateral expansion slows and R_{ax} will increase as the source continues to expand linearly.

We also found that Qs are significantly more asymmetric than NLRGs. The data suggest environmental factors are a predominant cause as there was no strong evidence for a contribution from relativistic effects, in contrast to the findings of AL00. However, stronger support for relativistic contributions to the BLRG x_{jet} distribution despite the finding that the BLRGs are not significantly more asymmetric than the low-power NLRGs. The implications for unification are discussed below.

6.4 Unification

We begin by noting that the classification of the sources into the broad and narrow line types is dependent on high-quality spectra. For example, Laing et al. (1994) have shown that the classifications may change significantly with improved observations. The classifications that we use are the best possible with the available data, but incorrect identification of some sources may introduce a bias that is difficult to estimate.

The unification model for Qs, NLRGs and BLRGs makes a

Table 11 continued.

Proposition	Conclusion	Details	Section
Is there a significant tendency toward higher p_j in Qs and BLRGs than in NLRGs?	Yes	Peto-Prentice test compared Qs and BLRGs with NLRGs. Significant at the 99.6 per cent confidence level.	section 4.3.2
Is there a tendency for p_j to be correlated with p_c ?	Yes	Linear regression gives Kendall's τ correlation coefficient as 3.5, significant correlation above the 99.9 per cent confidence level.	section 4.3.3
Do jetted sources have significantly more prominent cores?	Yes	Peto-Prentice test compared sources with definite or possible jets to those with no jet detection. Significant at 99.9 per cent confidence level.	section 4.3.3
Is there a tendency for the fractional hotspot size to be similar for each lobe within a source?	Yes	Linear regression gives Kendall's τ correlation coefficient as 5.5, significant above 99.9 per cent confidence level.	section 5.1.2
Is there a significant difference in the f_h distribution across the size range?	Yes	K-S test of f_h binned by LLS_s using cutoff of 200 kpc showed difference above 99.9 per cent confidence level.	section 5.1.2
Is there a significant difference in the f_h distribution across the luminosity range?	No	K-S test of f_h binned by P_{178} using a cutoff of $5 \cdot 10^{26} \text{ W Hz}^{-1} \text{ sr}^{-1}$ showed a difference significant at the 93.2 per cent confidence level	section 5.1.2
Is there a tendency for the more compact hotspot in a source to be correlated with jet side in Qs?	Yes	Binomial test shows relatively more compact hotspot tends to be on the jet-side at the 99.4 per cent confidence level.	section 5.1.2
Is there a tendency for smaller sources to have lower source recession coefficients?	Yes	K-S test ζ significantly lower in small source 99.7 per cent confidence level	section 5.2.3
Is there a tendency for Qs and BLRGs to have lower source recession coefficients ζ ?	No	W-M-W test compared Qs and high-power NLRGs and BLRGs and low-power NLRGs. Null hypothesis rejected at 74 and 84 per cent confidence level respectively.	section 5.2.3
Is there a significant difference in the distribution of ζ between different spectral classes?	No	K-S test compared Qs and high-power NLRGs and BLRGs and low-power NLRGs. Null hypothesis rejected at 94.5 and 81 per cent confidence level.	section 5.2.3

number of simple predictions. We expect Qs and BLRGs to be seen at smaller angles to the line of sight; this means that they should be more commonly associated with brighter, one-sided jets and brighter cores and should be statistically smaller, with lower R_{ax} as a consequence. There is no expectation that lobe size asymmetries should be significantly different from class to class, unless source expansion speeds are relativistic in which case the Qs and BLRGs would be expected to appear more asymmetrical.

As discussed in Section 6.2, Qs and BLRGs do have higher detection rates for kpc-scale jets, consistent with the expectation from unification. On the other hand, there is no significant trend for either spectral class to have quantitatively brighter jets than those in the NLRG, but the effects of observing resolution and sensitivity are not negligible and are difficult to account for.

The core prominence is found to be statistically higher in Qs than in high power NLRGs (Section 4.3.1) though the results for the much smaller sample of BLRGs and low-power NLRGs were less clear-cut. In fact, we found that the core prominence in NLRGs decreased with increasing source luminosity, which explains the quantitative difference between the high-luminosity spectral classes and the lack of it between those at low luminosity. This trend in the NLRG core prominence data is not obviously predicted from unification. However, we argued in Section 4.3.1 that this is evidence that the higher-luminosity sources may have higher nuclear bulk Lorentz factors (γ), leading to greater Doppler suppression of core emission: if the parsec-scale bulk-flow speeds of the emitting material are greater in the higher luminosity sources, the

cores of a greater proportion of the NLRGs could be Doppler suppressed, as the angle to the observer's line-of-sight needed to detect beamed emission would be smaller. This would represent a minor modification to the standard unification picture.

Considering source morphology, we found the Qs to have significantly lower R_{ax} values than the NLRGs (Section 3.2.3). However, in unified models we expect this to be a result of projection effects giving systematically lower source linear sizes. We found no evidence that either Qs or BLRGs are significantly smaller than the NLRGs. Although this could indicate that the statistically lower R_{ax} values in Qs are a result of relatively broader lobes (unexpected in the unified model), this does not appear to be the case and we concluded in section 3.2.3 that the difference in R_{ax} between the Qs and NLRGs was not inconsistent with projection effects, with smaller lobe sizes in Qs for a similar lobe width (Fig. 9). The fact that we did not obtain a similar result for the low-luminosity spectral classes might indicate a real difference between the high and low luminosity classes, although there was no trend in R_{ax} across the luminosity or redshift range and we found that the low power distribution is possibly more strongly affected by observational effects, with data from a few particularly small and large sources observed at low resolution (Fig. 10).

On the other hand, evidence for real differences in the Q environments is provided by the distribution of the fractional separation difference as defined by the longer lobe, x_{lobe} (Section 3.3.2). These data show that Qs are significantly more asymmetric than the high power NLRGs. This is not expected from unification directly.

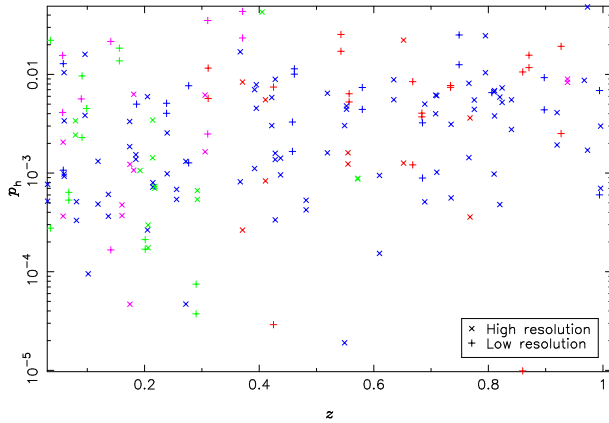


Figure 31. The hotspot prominence, p_h , of the primary hotspot plotted against z , binned by high-resolution effective observing resolution. Diagonal cross: effective observing resolution > 100 , vertical cross: effective observing resolution ≤ 100 . Green: low excitation radio galaxies, blue: narrow line radio galaxies, magenta: broad line radio galaxies and red: quasars (on-line colour version).

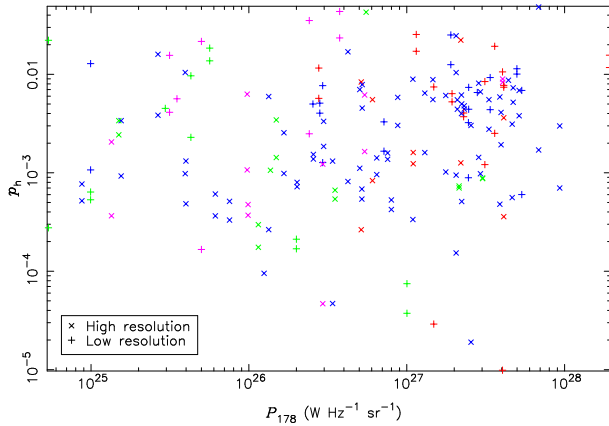


Figure 32. The hotspot prominence, p_h , of the primary hotspot plotted against the source luminosity, binned by high-resolution effective observing resolution. Diagonal cross: effective observing resolution > 100 , vertical cross: effective observing resolution ≤ 100 . Green: low excitation radio galaxies, blue: narrow line radio galaxies, magenta: broad line radio galaxies and red: quasars (on-line colour version).

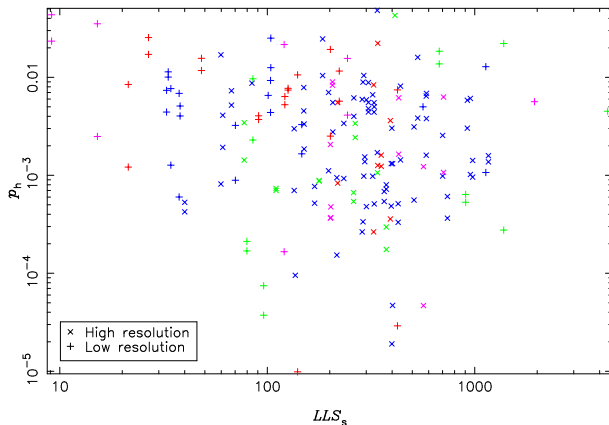


Figure 33. The hotspot prominence, p_h , of the primary hotspot plotted against the lobe size, binned by high-resolution effective observing resolution. Diagonal cross: effective observing resolution > 100 , vertical cross: effective observing resolution ≤ 100 . Green: low excitation radio galaxies, blue: narrow line radio galaxies, magenta: broad line radio galaxies and red: quasars (on-line colour version).

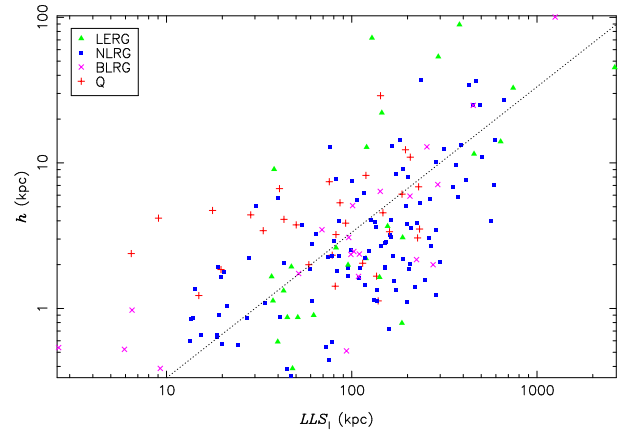


Figure 34. The linear hotspot size, h , plotted against the largest linear size of the lobe, LLS_1 . The dotted line has slope unity.

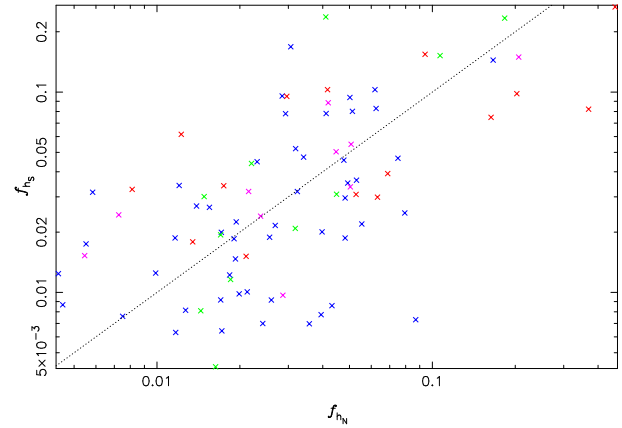


Figure 35. The S lobe fractional hotspot size, f_{hS} , plotted against the N lobe fractional hotspot size, f_{hN} . Green: low excitation radio galaxies, blue: narrow line radio galaxies, magenta: broad line radio galaxies and red: quasars (on-line colour version). The dotted line indicates $f_{hS} = f_{hN}$.

It could be consistent with the scheme if relativistic effects were contributing to the observed lobe size asymmetry, which would require relativistic source advance speeds; however, assuming that the kpc-scale jet indicates the approaching lobe and re-defining the fractional separation in terms of the jet-side lobe, x_{jet} , no significant differences were found between any of the spectral classes, so that there is no evidence for the hypothesis that the greater asymmetry of the quasars is due to relativistic effects. This then suggests that the effect is environmental, though of course, as not all sources have jets, the x_{jet} data do not include all sample sources and so will be biased.

7 SUMMARY AND CONCLUSION

A large complete sample of FR II type radio sources has been studied with high sensitivity, high resolution observations, allowing standard models of unification and relativistic beaming to be tested. The sample consists of 98 sources from the 3CRR sample with $z < 1$, including 15 Qs, 11 BLRGs and 57 NLRGs, as well as 15 LERGs, and covers a large range in source luminosity (from 5×10^{24} to 2×10^{28} $W Hz^{-1} sr^{-1}$ at 178 MHz). The high quality of the maps has allowed a comprehensive search for trends and corre-

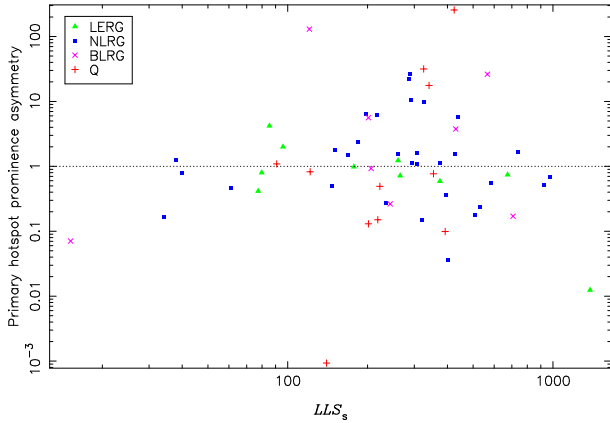


Figure 36. The hotspot flux ratio as defined by jet side plotted against the largest linear lobe size, LLS_s . The dotted line shows a ratio of unity.

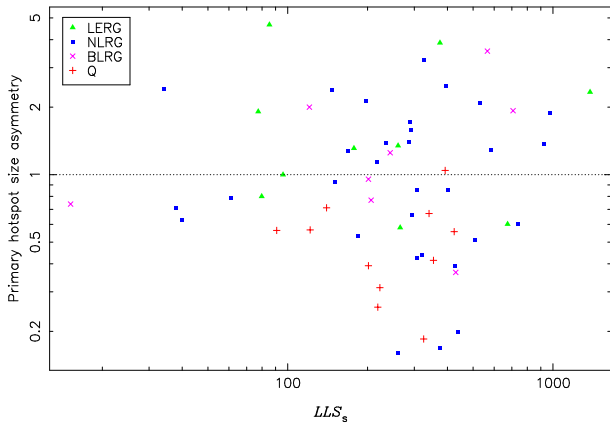


Figure 37. The ratio of the fractional hotspot size, f_h , for the primary hotspot in each lobe as defined by jet side, plotted against the largest linear lobe size, LLS_s . The dotted line shows a ratio of unity.

lations between source observables, with source sizes, axial ratios, core, jet and hotspot properties measured from the same observed data.

We have searched for differences in the distributions of the various source observables with respect to the sample’s range in power, redshift and source size, and carried out tests of the predictions of the standard model of unification and relativistic beaming. These predictions are that Qs and BLRGs will be statistically smaller, with higher jet detection rates and brighter jets and cores. In addition, there is some weaker evidence that hotspot properties, such as compactness, may be correlated with the jet side, which implies that there is continued relativistic flow in the hotspot regions.

Some evidence for differences in the sample as a function of luminosity were found:

- core prominence was found to decrease with source luminosity. We proposed that a greater proportion of higher luminosity sources have higher parsec-scale bulk flow speeds and experience stronger Doppler suppression: this can be accommodated as a modification to standard unified models.
- Qs are found to be more asymmetric than the high power NLRGs and the evidence is that this is not due to relativistic effects; also no such difference is found between BLRGs and NLRGs. This is possible evidence that there is a systematic difference between

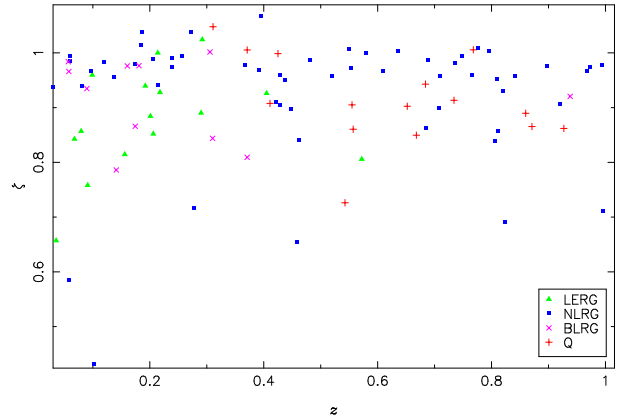


Figure 38. The source hotspot recession coefficient, ζ , plotted against z .

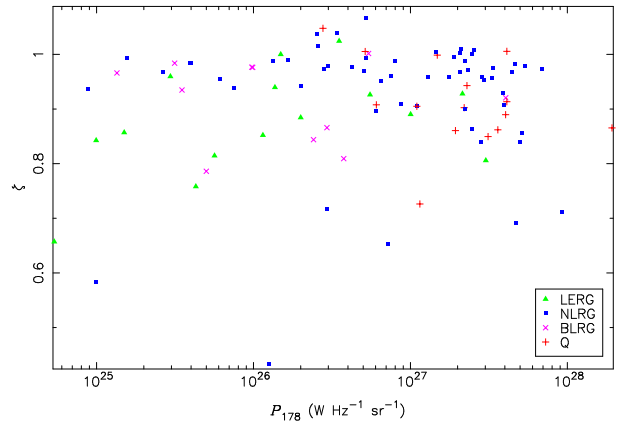


Figure 39. The source hotspot recession coefficient, ζ , plotted against P_{178} .

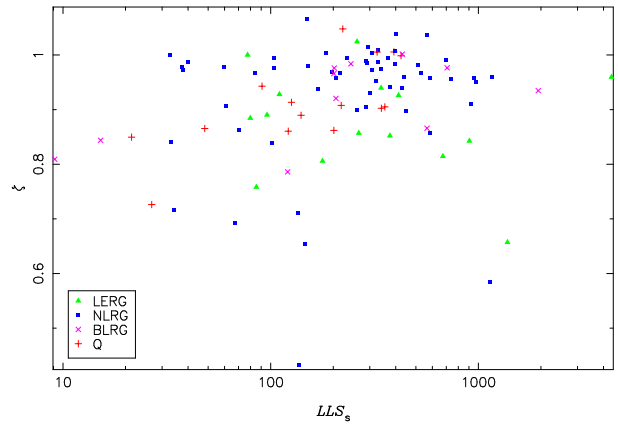


Figure 40. The source hotspot recession coefficient, ζ , plotted against LLS_s .

the environments of Qs and NLRGs at high radio luminosities, which would not be consistent with simple unification models.

The principal conclusions *consistent* with the predictions of the standard model can be summarized as follows.

- evidence for beaming on kiloparsec scales was found across the sample; jet detection rates as a function of source class, correlation between core and jet prominence and detections of the Laing-Garrington effect were all consistent with relativistic speeds in the kpc-scale jets.

- cores were found to be statistically brighter in Qs and BLRGs than in the corresponding NLRGs, consistent with expectations.

- R_{ax} values were found to be lower in Qs (although not BLRGs) than those in the corresponding population of NLRG, consistent with the expected projection effects.

A further result somewhat independent from the expectations of the standard model was that

- there is evidence from the distribution of R_{ax} that source development has an initial phase where expansion is self-similar or close to being so, possibly on the scale of the host galaxy, before lateral expansion slows or ceases while the expansion along the source axis continues.

We will consider the implications of our measurements for quantitative estimates of the relativistic bulk speeds in cores and jets in a future paper (Mullin & Hardcastle, in prep.).

8 ACKNOWLEDGMENTS

LMM thanks PPARC for a research studentship that supported the early parts of this work. MJH thanks the Royal Society for a research fellowship.

REFERENCES

- Akujor, C. E., Garrington, S. T., 1995, 112, 235
 Arshakian, T. G., Longair, M. S., 2000, MNRAS, 311, 846 (AL00)
 Baars, J. W. M., Genzel, R., Pauliny-Toth, I. I. K., Witzel, A., 1977, A&A, 61, 99
 Banhatti, D. G., 1980, A&A, 84, 112
 Barthel, P. D., 1987, In *Superluminal Radio Sources*, p 148
 Barthel, P. D., 1989, ApJ, 336, 606
 Barthel, P. D., 1994, In *ASP Conf. Ser. 54: The Physics of Active Galaxies*, p 175
 Begelman, M. C., Cioffi, D. F., 1989, 345, L21
 Bennett, A. S., 1962, MNRAS, 68, 163
 Best, P. N., Bailer, D. M., Longair, M. S., Riley, J. M., 1995, MNRAS, 275, 1171
 Black, A. R. S., Baum, S. A., Leahy, J. P., Perley, R. A., Riley, J. M., Scheuer, P. A. G., 1992, MNRAS, 256, 186
 Blundell, K. M., Rawlings, S., Willott, C. J., 1999, AJ, 117, 677
 Bridle, A. H., Hough, D. H., Lonsdale, C. J., Burns, O. J., Laing, R. A., 1994, AJ, 108, 766
 Bridle, A. H., Perley, R. A., 1984, ARA&A, 22, 319
 Carvalho, J. C., O'Dea, C. P., 2002, ApJS, 141, 371
 Chambers, K. C., Miley, G. K., van Breugel, W., 1987, Nature, 329, 604
 Chiaberge, M., Capetti, A., Celotti, A., 2002, A&A, 394, 791
 Clarke, D. A., Bridle, A. H., Burns, J. O., Perley, R. A., Norman, M. L., 1992, ApJ, 385, 173
 Conway, R. G., Birch, P., Davis, R. J., Jones, L. R., Kerr, A. J., Stannard, D., 1983, MNRAS, 202, 813
 Dennett-Thorpe, J., Barthel, P. D., van Bemmell, I. M., 2000, A & A, 364, 501
 Dennett-Thorpe, J., Bridle, A. H., Laing, R. A., Scheuer, P. A. G., 1999, MNRAS, 304, 271
 Falle, S. A. E. G., 1991, MNRAS, 250, 581
 Fanaroff, B. L., Riley, J. M., 1974, MNRAS, 167, 31
 Fanti, C., Fanti, R., Dallacasa, D., Schilizzi, R. T., Spencer, R. E., Stanghellini, C., 1995, A & A, 302, 317
 Fernini, I., 2001, AJ, 122, 83
 Fernini, I., Burns, J. O., Bridle, A. H., Perley, R. A., 1993, AJ, 105, 1690
 Fernini, I., Burns, J. O., Perley, R. A., 1997, AJ, 114, 2292
 Fernini, I., Leahy, J. P., Burns, J. O., Basart, J. P., 1991, AJ, 381, 63
 Garrington, S. T., Conway, R. G., 1991, MNRAS, 250, 198
 Garrington, S. T., Conway, R. G., Leahy, J. P., 1991, MNRAS, 250, 171
 Garrington, S. T., Leahy, J. P., Conway, R. G., Laing, R. A., 1988, Nature, 331, 147
 Gilbert, G. M., Ph.D. thesis, University of Cambridge, 2001
 Gilbert, G. M., Riley, J. M., 1999, MNRAS, 309, 681 (G99)
 Gilbert, G. M., Riley, J. M., Hardcastle, M. J., Croston, J. H., Pooley, G. G., Alexander, P., 2004, MNRAS, 351, 845
 Goodlet, J. A., Kaiser, C. R., Best, P. N., Dennett-Thorpe, J., 2004, MNRAS, 347, 508
 Hardcastle, M. J., 2004, A&A, 414, 927
 Hardcastle, M. J., Alexander, P., Pooley, G. G., Riley, J. M., 1997, MNRAS, 288, 859
 Hardcastle, M. J., Alexander, P., Pooley, G. G., Riley, J. M., 1998, MNRAS, 296, 445 (H98)
 Hardcastle, M. J., Evans, D. A., Croston, J. H., 2006, MNRAS, 370, 1893
 Hardcastle, M. J., Worrall, D. M., 2000, MNRAS, 319, 562
 Hine, R. G., Longair, M. S., 1979, MNRAS, 188, 111, 130
 Hough, D. H., Wing, N., Linick, J. P., Escobedo, S. M., Legal, K. E., Lester, W. R., 2002, AAS, 200, 0507
 Inskip, K. J., Best, P. N., Röttgering, H. J. A., Rawlings, S., Cotter, G., Longair, M. S., 2002, MNRAS, 337, 1407
 Johnson, R. A., Leahy, J. P., Garrington, S. T., 1995, MNRAS, 273, 877
 Kaiser, C. R., Alexander, P., 1997, MNRAS, 286, 215
 Kaiser C. R., Dennett-Thorpe, J., Alexander, P., 1997, MNRAS, 292, 723
 Katz-Stone, D. M., Rudnick, L., 1997, ApJ, 479, 258
 Kharb, P., O'Dea, C. P., Baum, S. A., Daly, R. A., Mory, M. P., Donahue, M., Guerra, E. J., Laing, R. A., 1988, Nature, 331, 149
 Laing, R. A., Peacock, J. A., 1980, MNRAS, 190, 903
 Laing, R. A., Riley, J. M. and Longair, M. S., 1983, MNRAS, 204, 151 (LRL)
 Laing, R. A., 1989, Lecture Notes in Physics, Springer Verlag, Berlin, 327:27-43
 Laing, R. A., Jenkins, C. R., Wall, J. V., Unger, S. W., 1994, In *ASP Conf. Ser. 54: The Physics of Active Galaxies*, p 201
 LaValley M., Isobe T., Feigelson E. D., 1992, BAAS, 24, 839
 Leahy, J. P., Black, A. R. S., Dennett-Thorpe, J., Hardcastle, M. J., Komissarov, S., Perley, R. A., Riley, J. M., Scheuer, P. A. G., 1997, MNRAS, 291, 20
 Leahy, J. P., Perley, R. A., 1991, ApJ, 102, 2
 Leahy, J. P., Williams, A. G., 1994, MNRAS, 210, 929
 Lui, R., Pooley, G., 1991, 249, 343
 McCarthy, P. J., van Breugel, W., Spinrad, H., Djorgovski, S., 1987, ApJ, 321, L29
 Mullin, L. M., Hardcastle, M. J., Riley, J. M., 2006, MNRAS, 372, 113
 Pedalty, J. A., Rudnick, L., McCarthy, P. J., Spinrad, H., 1989, 97, 647
 Privon, G. C., O'Dea, C. P., Baum, S. A., Axon, D. J., Kharb, P., Buchanan, C. L., Sparks, W., Chiaberge, M., 2008, ApJS, 175,

473

Roettiger, K., Burns, J. O., Clarke, D. A., Christiansen, W. A.,
1994, ApJ, 421, L23

Rudnick, L., 1988, ApJ, 325, 189

Rudnick, L., Anderson, M., 1990, ApJ, 355, 427

Scheuer, P. A. G., 1987, In *Superluminal Radio Sources*, p 104

Scheuer, P. A. G., 1995, MNRAS, 277, 33

Scheuer, P. A. G., Readhead, A. C. S., 1979, Nature, 277, 182

Taylor, G. B., Jingping, G., O'Dea, C. P., 1995, AJ, 110, 522

van Breugel, W. J., Dey, A., 1993, ApJ, 414, 563

Wright, M. C. H., 1979, ApJ, 228, 34

Zensus, J. A., 1997, ARA&A, 35, 607

Table 12: Core and jet properties

Source name	Core prominence ($\times 1000$)		Jet side	Jet prominence ($\times 1000$)		C'jet prominence ($\times 1000$)		position	Fractional jet	
	value	error		value	error	value	error		length	termination
4C12.03	<9		N	31	2	42	4	–	0.3223	0.3223
3C6.1	7.46	0.2	S	<18.6		<1.0		–	–	–
3C16	0.23	0.010	N	3.6	0.2	2.4	0.2	0.0539	0.195	0.249
3C19	0.33	0.08	S	17	3	<23.0		0.642	0.29	0.93
3C20	3.3	0.6	N	7	5	<9.0		0.178	0.7421	0.921
3C22	6.54	0.2	N	4.2	0.9	<4.0		–	0.7568	0.7568
3C33	36.2	1	S	42	3	20	7	–	0.2611	0.2611
3C33.1	12.2	0.4	S	27.0	0.8	<37.0		–	0.5252	0.5252
3C34	1.04	0.03	N	7.3	0.2	1.1	0.10	0.472	0.606	1.08
3C35	18.6	0.05	N	<12		<15		–	–	–
3C41	1.2	0.04	S	13	0.6	<21.0		0.207	0.721	0.929
3C42	3.05	0.09	S	<24.8		<17.8		–	–	–
3C46	1.44	0.04	S	1.4	0.10	<5.9		0.20	0.39	0.59
3C47	66.8	2	S	12	2	<1.1		–	0.7238	0.7238
3C55	5.33	0.2	S	10	4	<36.0		–	0.291	0.291
3C61.1	2.2	0.07	N	<58.2		<26.9		–	–	–
3C67	2.13	0.06	N	45	8	<14.8		0.39	0.23	0.63
3C79	6.04	0.2	N	<3.8		<1.3		–	–	–
3C98	6.10	0.2	N	50	20	<13.0		–	0.8676	0.8676
3C109	247	7	S	25	2	<8.8		0.6250	0.198	0.823
4C14.11	29.7	0.9	N	11	0.4	<11.0		0.7247	0.2543	0.9790
3C123	109	3	S	<30.0		<2.1		–	–	–
3C132	4.1	0.2	S	3	2	<13.0		0.148	0.553	0.701
3C153	<0.5		S	10	5	8.0	0.2	0.21	0.412	0.62
3C171	2.0	0.10	S	6.3	0.8	6.0	0.2	–	0.762	0.762
3C172	0.37	0.02	S	<25.0		<3.6		–	–	–
3C173.1	9.64	0.3	N	2.1	0.10	<0.3		–	0.3739	0.3739
3C175	14.0	0.4	S	6.3	0.3	<10.6		–	0.6460	0.6460
3C175.1	1.1	0.08	S	75	10	<15.1		0.652	0.24	0.89
3C184	0.11	0.07	N	<47.2		<37.4		–	–	–
3C184.1	6.0	0.5	N	3.9	0.7	<5.9		0.4354	0.3048	0.7401
DA240	273	8	S	83	10	<23.0		–	0.4248	0.4248
3C192	4.0	0.2	S	8.0	0.2	<3.2		0.765	0.150	0.915
3C196	11.8	0.4	S	<58.4		<46.3		–	–	–
3C200	38.2	1	S	60	8	<1.0		–	0.7279	0.7279
4C14.27	11.4	0.3	N	16	3	6.1	0.9	–	0.4896	0.4896
3C207	539	20	S	190	10	<43.9		–	0.695	0.695
3C215	0.88	0.10	S	38.4	1	<2.8		–	0.8325	0.8325
3C217	0.69	0.02	N	<12.3		<2.1		–	–	–
3C216	732	20	S	<5.3		–		–	–	–
3C219	51.6	2	S	56.5	0.3	2.1	0.10	0.0203	0.1677	0.188
3C220.1	26.9	0.8	N	3.6	0.10	<9.5		0.103	0.8071	0.910
3C220.3	<0.2		N	<2.9		<1.5		–	–	–
3C223	8.50	0.3	N	10	4	6	9	0.6459	0.1899	0.8358
3C225B	1.3	0.10	N	<4.2		<2.9		–	–	–
3C226	3.71	0.10	S	<3.8		<3.1		–	–	–
4C73.08	7	1	S	<615.3		<87.2		–	–	–
3C228	19.0	0.6	S	10.7	0.3	<15.0		0.141	0.316	0.457
3C234	34.5	1	N	10	8	<19.0		–	0.0965	0.0965
3C236	5170	2×10^2	N	290	50	<61.9		0.00450	0.3860	0.390
4C74.16	1.61	0.05	S	9.7	1	<5.4		–	0.5702	0.5702
3C244.1	1	0.7	N	3.2	1	<13.4		0.7361	0.244	0.980
3C247	1.81	0.05	N	<2.1		<1.6		–	–	–
3C249.1	70.7	2	N	35	5	<9.9		–	0.289	0.289
3C254	20.0	0.6	N	<10.3		<6.3		–	–	–
3C263	161	5	S	39	5	<1.7		–	0.8970	0.8970
3C263.1	1.4	0.05	N	<1.2		<0.5		–	–	–

Table 12: Core and jet properties

Source name	Core prominence ($\times 1000$)		Jet side	Jet prominence ($\times 1000$)		C'jet prominence ($\times 1000$)		Fractional jet		
	value	error		value	error	value	error	position	length	termination
3C265	2.78	0.08	N	4.8	1	<5.3		–	0.6910	0.6910
3C268.1	0.45	0.04	S	<4.1		<1.9		–	–	–
3C268.3	1.2	0.09	S	<25.0		<7.5		–	–	–
3C274.1	2.33	0.07	S	8	8	<20.9		–	0.7585	0.7585
3C275.1	209	6	N	30	20	<4.6		–	0.681	0.681
3C277.2	0.68	0.02	S	17	4	<2.2		–	0.327	0.327
3C280	<0.7		S	<13.8		<0.4		–	–	–
3C284	2.79	0.08	S	<6.6		<2.8		–	–	–
3C285	6.49	0.2	N	7.8	1	<19.9		0.071	0.89	0.96
3C289	0.78	0.08	N	<4.8		2	1	–	–	–
3C292	0.51	0.03	S	<5.9		<3.9		–	–	–
3C295	3.64	0.10	N	<230.5		<118.9		–	–	–
3C299	2.3	0.2	N	<11.8		<21.2		–	–	–
3C300	6.20	0.2	N	2.4	0.10	<0.2		–	0.9148	0.9148
3C303	106	3	N	63.0	2	<13.0		–	0.5108	0.5108
3C319	<0.3		S	<1.8		<0.10		–	–	–
3C321	23.1	0.7	N	15	1	–		0.00942	0.1258	0.135
3C325	10.1	0.3	N	5.8	0.9	<25.3		0.123	0.633	0.755
3C326	18.2	0.6	S	<215.3		<25.8		–	–	–
3C330	0.54	0.02	S	<34.0		<21.5		–	–	–
3C334	86.8	3	S	17	1	0.2	0.2	–	0.5630	0.5630
3C336	21.3	0.6	S	7.7	0.7	<14.9		–	0.464	0.464
3C341	0.70	0.03	S	22	2	<7.4		–	0.438	0.438
3C337	0.34	0.03	S	3.2	0.10	<4.4		0.0876	0.6836	0.771
3C340	1.16	0.03	S	<6.0		<3.6		–	–	–
3C349	24.2	0.7	S	0.31	0.04	<2.1		0.0826	0.0245	0.107
3C351	12.1	0.4	N	5.3	2	<0.9		–	0.0864	0.0864
3C352	3.38	0.10	N	8.9	0.7	<9.4		–	0.542	0.542
3C381	4.70	0.10	N	<2.9		<1.3		–	–	–
3C382	251	8	N	14	1	<1100.0		–	0.88	0.88
3C388	57.1	2	S	17	1	<5.3		–	0.661	0.661
3C390.3	733	20	N	20	10	<650.0		–	0.6298	0.6298
3C401	28.5	0.9	S	33.8	0.4	<5.7		–	0.8903	0.8903
3C427.1	0.89	0.03	N	20	10	<16.5		0.612	0.351	0.963
3C433	1.2	0.3	N	9.8	0.10	<8.3		–	0.594	0.594
3C436	17.9	0.5	S	3.8	0.8	<0.3		0.101	0.7804	0.881
3C438	16.2	0.5	N	40	4	<9.8		–	0.757	0.757
3C441	<0.10		N	23	2	<10.4		–	0.787	0.787
3C452	126	4	S	13	2	9.0	2	–	0.7547	0.7547
3C455	<2.6		S	<30.8		<18.1		–	–	–
3C457	2.32	0.07	S	<5.4		<5.2		–	–	–

Table 13: Hotspot properties

Source	N hotspot properties				S hotspot properties				Recession properties	
	prominence ($\times 1000$)	size (arcsec)	frac. size	η	prominence ($\times 1000$)	size (arcsec)	frac. size	η	ζ	δ
4C12.03	13.7	19.88	0.1831	0.9587	18.5	33.03	0.2340	0.6186	0.8145	0.6452
3C6.1	5.53	0.25	0.017	0.9493	2.77	0.25	0.020	0.9665	0.9572	1.018
3C16	–	–	–	0.881	42.9	13.3	0.562	1.027	0.926	1.17
3C19	0.5	0.17	0.049	1.12	0.42	0.1	0.04	0.838	0.988	0.746
3C20	3.3	0.18	0.0075	0.9670	1.9	0.20	0.0076	0.9926	0.9794	1.026
3C22	8.31	0.30	0.022	0.9762	8.97	0.39	0.032	0.8576	0.9206	0.8785
3C33	0.979	0.63	0.0045	0.9865	10.4	1.0	0.0087	0.9829	0.9849	0.9964
3C33.1	6.29	4.23	0.0507	0.978	1.07	8.16	0.0549	0.9758	0.977	1.00
3C34	5.01	1.85	0.0794	0.966	0.511	0.57	0.025	1.01	0.988	1.05
3C35	0.64	–	–	0.9355	0.53	8.90	0.0252	0.7511	0.8426	1.245
3C41	10.4	1.0	0.075	0.9701	24.7	0.53	0.047	1.040	1.003	1.072
3C42	4.54	0.42	0.031	1.040	7.87	2.4	0.17	1.092	1.066	0.9528
3C46	1.42	1.2	0.012	0.92	0.958	2.34	0.034	0.99	0.95	1.1
3C47	0.029	2.21	0.0632	1.034	7.44	1.2	0.030	0.9815	0.9986	1.054
3C55	3.12	0.42	0.012	0.9903	0.559	0.21	0.0063	0.9734	0.9822	0.9830
3C61.1	5.00	11.9	0.157	1.11	–	–	–	0.9882	1.04	1.12
3C67	2.5	0.08	0.04	0.882	35.2	0.12	0.088	0.785	0.844	0.890
3C79	0.683	0.80	0.020	1.013	0.541	0.51	0.0098	0.9792	0.9941	1.035
3C98	0.77	3.75	0.0269	0.9558	0.52	2.95	0.0216	0.9173	0.9368	0.9597
3C109	1.65	1.31	0.0287	1.016	6.18	0.48	0.0097	0.9887	1.002	1.027
4C14.11	0.175	0.91	0.016	1.035	0.297	0.24	0.0043	0.6680	0.8522	0.6455
3C123	0.70	0.26	0.014	0.913	0.734	0.1	0.008	0.941	0.928	0.970
3C132	3.44	0.17	0.015	1.002	1.4	0.33	0.030	0.9981	1.000	0.9964
3C153	7.68	0.1	0.03	0.51	1.3	0.33	0.096	1.01	0.72	2.0
3C171	5.1	0.2	0.03	0.996	4.04	0.24	0.047	0.950	0.973	0.954
3C172	6.44	1.64	0.0357	1.01	1.60	0.34	0.0070	0.911	0.958	1.11
3C173.1	0.666	0.51	0.019	1.072	0.54	0.38	0.012	0.9886	1.024	1.084
3C175	3.62	0.46	0.021	1.003	0.358	0.47	0.015	1.007	1.006	0.9960
3C175.1	4.10	0.14	0.032	0.982	1.93	0.11	0.032	0.814	0.907	0.830
3C184	0.601	0.07	0.02	0.974	6.86	0.08	0.04	0.988	0.979	1.01
3C184.1	0.48	1.80	0.0170	0.9814	1.3	0.72	0.0092	0.987	0.984	1.01
DA240	22.2	19.81	0.02203	0.7572	0.28	46.25	0.04405	0.571	0.657	1.33
3C192	3.4	3.50	0.0319	0.9840	0.927	4.83	0.0522	1.01	0.994	1.02
3C196	11.7	0.24	0.094	0.902	15.7	0.57	0.15	0.840	0.865	1.07
3C200	3.30	0.55	0.050	0.55	1.66	1.33	0.0940	0.7375	0.65	0.74
4C14.27	7.01	1.2	0.053	0.9479	1.11	0.55	0.036	1.001	0.9694	1.056
3C207	3.71	0.94	0.16	0.925	4.05	0.53	0.075	0.958	0.943	0.965
3C215	5.53	5.30	0.203	0.8588	0.832	1.36	0.0982	0.9978	0.9076	1.162
3C217	9.28	–	–	1.00	4.37	0.29	0.079	0.911	0.976	0.911
3C216	8.46	0.34	0.37	0.94	1.21	0.17	0.082	0.78	0.85	1.2
3C219	0.047	0.68	0.0073	0.8405	1.23	2.40	0.0244	0.8870	0.8660	0.9476
3C220.1	0.947	0.38	0.026	1.009	0.153	0.33	0.019	0.9323	0.9672	1.082
3C220.3	3.23	0.71	0.17	0.800	0.890	0.81	0.14	0.911	0.863	0.878
3C223	0.61	2.40	0.0155	0.9236	0.4	4.00	0.0266	0.9883	0.9558	1.070
3C225B	7.37	0.13	0.062	0.930	4.42	0.29	0.10	1.05	1.00	0.886
3C226	0.479	0.31	0.014	1.017	5.89	0.48	0.027	0.8560	0.9297	1.189
4C73.08	1.07	24.17	0.04114	0.3239	12.9	32.66	0.07814	0.9323	0.5843	2.879
3C228	4.44	0.48	0.019	0.9214	4.79	0.42	0.019	1.033	0.9719	1.121
3C234	1.54	0.35	0.0055	1.007	1.4	0.54	0.017	1.031	1.015	1.024
3C236	–	–	–	0.9141	4.51	24.77	0.01722	0.9966	0.9597	0.9172
4C74.16	6.64	1.2	0.048	0.9948	0.979	0.53	0.030	0.8880	0.9524	0.8927
3C244.1	8.93	0.34	0.013	1.009	0.335	0.20	0.0081	0.7867	0.9046	0.7798
3C247	12.5	0.28	0.048	1.00	25.1	0.38	0.046	0.989	0.995	1.01
3C249.1	5.70	0.36	0.012	1.74	11.6	1.17	0.0615	0.7924	1.05	2.19
3C254	7.41	0.53	0.042	0.9199	7.72	0.47	0.10	0.877	0.913	0.954
3C263	1.26	0.44	0.013	0.8526	22.3	0.30	0.018	1.001	0.9025	1.174
3C263.1	7.30	0.23	0.087	0.937	5.20	0.04	0.007	0.584	0.692	1.60

Table 13: Hotspot properties

Source	N hotspot properties				S hotspot properties				Recession properties	
	prominence ($\times 1000$)	size (arcsec)	frac. size	η	prominence ($\times 1000$)	size (arcsec)	frac. size	η	ζ	δ
3C265	3.80	0.90	0.019	0.7714	6.87	0.70	0.023	0.9823	0.8564	1.273
3C268.1	48.2	0.28	0.012	0.9945	1.71	0.35	0.019	0.9484	0.9739	0.9536
3C268.3	43.5	0.1	0.2	0.67	23.4	0.19	0.15	0.869	0.81	0.77
3C274.1	5.83	4.54	0.0512	0.8866	3.03	6.21	0.0802	0.9375	0.9101	1.057
3C275.1	5.26	0.36	0.030	0.804	6.37	0.64	0.095	0.960	0.861	1.19
3C277.2	1.43	1.7	0.040	0.9439	8.13	0.33	0.020	0.9976	0.9595	1.057
3C280	0.700	0.06	0.006	0.594	2.99	0.24	0.032	0.849	0.711	1.43
3C284	0.983	2.02	0.0184	0.9756	2.55	0.92	0.012	1.011	0.9900	1.036
3C285	2.43	8.55	0.11	0.79	3.38	14.74	0.152	0.91	0.86	0.86
3C289	–	–	–	0.963	8.72	0.1	0.02	0.971	0.967	1.01
3C292	1.02	3.48	0.0554	0.9195	6.10	1.54	0.0220	0.9921	0.9586	0.9268
3C295	10.1	0.15	0.062	0.841	11.4	0.28	0.083	0.840	0.840	1.00
3C299	17.0	0.1	0.04	0.980	0.82	0.07	0.009	0.977	0.978	1.00
3C300	0.05	0.30	0.0044	1.027	1.3	0.35	0.012	1.068	1.039	1.039
3C303	21.6	1.40	0.0504	0.648	0.17	0.70	0.034	1.00	0.786	1.54
3C319	1.1	1.1	0.024	1.006	–	–	–	0.8832	0.9397	1.139
3C321	3.84	3.16	0.0213	1.000	16.0	1.51	0.0101	0.9349	0.9677	0.9349
3C325	0.0099	0.18	0.017	0.894	10.6	0.26	0.034	0.883	0.890	0.988
3C326	–	–	–	0.9827	5.64	60.16	0.08020	0.9094	0.9348	1.081
3C330	0.019	0.79	0.026	0.9817	3.03	0.29	0.0092	1.032	1.007	0.9510
3C334	1.61	1.7	0.053	0.8915	1.24	0.70	0.031	0.9256	0.9049	1.038
3C336	19.3	1.0	0.069	1.005	2.51	0.41	0.039	0.654	0.862	0.650
3C341	–	–	–	0.867	–	–	–	0.938	0.897	1.08
3C337	5.54	0.56	0.019	1.042	8.84	0.23	0.015	0.9342	1.004	0.8968
3C340	4.42	1.1	0.048	0.9865	5.51	0.39	0.019	1.035	1.009	1.049
3C349	0.26	0.40	0.0099	1.006	5.9	0.56	0.012	0.9721	0.9884	1.035
3C351	8.36	0.22	0.0081	0.9937	0.264	1.2	0.033	1.013	1.005	0.9807
3C352	6.54	0.50	0.070	0.699	–	–	–	0.989	0.839	1.41
3C381	0.48	0.18	0.0055	0.9911	0.37	0.60	0.015	0.9631	0.9761	1.029
3C382	2.1	2.10	0.024	0.97	0.37	2.20	0.024	0.96	0.97	0.98
3C388	2.29	1.15	0.0410	0.719	9.66	5.34	0.237	0.800	0.758	1.11
3C390.3	4.12	5.78	0.0447	0.9846	15.6	4.61	0.0504	0.983	0.984	0.998
3C401	0.2	0.50	0.045	0.825	0.2	0.40	0.031	0.9351	0.884	0.882
3C427.1	0.873	0.40	0.032	0.930	0.885	0.30	0.021	0.697	0.806	1.33
3C433	–	–	–	0.793	0.10	0.60	0.018	0.17	0.43	4.8
3C436	0.72	2.28	0.0394	0.9803	0.800	0.39	0.0077	0.8948	0.9416	0.9128
3C438	0.07	0.20	0.017	0.9454	0.04	0.20	0.019	0.830	0.890	0.878
3C441	6.17	0.32	0.029	0.715	4.00	1.99	0.0780	0.973	0.899	0.735
3C452	0.3	2.35	0.0172	0.9969	0.51	0.92	0.0064	0.8857	0.9389	1.125
3C455	17.2	0.66	0.46	0.63	25.5	0.74	0.27	0.773	0.73	0.82
3C457	1.59	2.58	0.0242	0.9604	1.37	0.71	0.0070	0.9587	0.9596	0.9982

Table 14: Lobe properties

Source	North lobe					South lobe					χ_{lobe}
	LLS_1 (kpc)	l (kpc)	RC (kpc)	f_1	R_{ax}	LLS_1 (kpc)	l (kpc)	RC (kpc)	f_1	R_{ax}	
4C12.03	293.3	293.3	16.5	1.00	2.511	381.2	215.7	8.26	1.00	2.856	0.1304
3C6.1	111.4	111.4	9.08	0.89	2.87	95.62	95.62	8.78	0.83	2.38	0.07630
3C16	284	284	13.5	0.98	3.23	128.6	128.6	20.3	1.00	1.58	0.377
3C19	21.2	20.5	2.8	1.00	1.57	18.7	18.4	3.6	1.00	1.57	0.0629
3C20	72.83	71.50	5.02	1.00	1.871	77.76	67.63	4.87	1.00	2.520	0.03275
3C22	109.9	109.1	6.5	0.51	4.06	96.30	96.30	7.3	0.48	1.83	0.06575
3C33	159.4	159.4	1.64	0.26	4.93	132.6	132.6	1.64	0.29	3.640	0.09179
3C33.1	254	254	12.7	1.00	1.29	452.8	436.8	9.54	0.94	2.81	0.281
3C34	165	165	8.5	0.98	2.22	162	151	8.88	1.00	2.9	0.00953
3C35	447.7	447.7	60.81	1.00	1.360	457.0	454.1	48.49	1.00	1.498	0.01032
3C41	99.87	95.15	7.87	0.75	2.49	84.96	84.96	8.69	1.00	1.81	0.08066
3C42	74.01	74.01	20.8	1.00	1.87	75.98	75.98	20.8	0.98	1.013	0.01315
3C46	588	588	12.3	0.83	4.7	390	390	19.4	0.83	2.9	0.20
3C47	194.8	105.7	6.80	0.83	1.410	229.4	219.4	12.0	0.70	1.741	0.08143
3C55	261.5	261.5	10.9	0.85	6.46	248.1	238.3	4.4	0.88	5.74	0.02644
3C61.1	236	236	13.1	1.00	4.42	327.3	327.3	13.9	1.00	3.35	0.162
3C67	9.25	9.25	0.3	1.00	2.03	5.93	5.93	0.4	1.00	0.942	0.219
3C79	160.0	160.0	11.3	1.00	1.585	206.2	206.2	11.0	0.99	2.324	0.1262
3C98	85.38	85.38	1.37	1.00	1.992	83.62	83.62	0.43	0.99	2.561	0.01040
3C109	206.2	206.2	16.0	0.77	2.183	223.8	223.8	18.3	1.00	2.388	0.04081
4C14.11	188.2	188.2	12.4	0.99	1.972	186.6	186.6	10.1	0.99	2.817	0.004324
3C123	62.30	28.7	3.81	0.58	1.077	47.85	34.43	4.62	0.73	0.9483	0.1312
3C132	39.85	39.85	2.5	1.00	5.07	37.56	37.56	2.4	0.82	1.59	0.02965
3C153	20	20	1.1	0.57	1.4	14.3	14.3	1.6	1.00	1.73	0.16
3C171	18.8	18.6	2.9	1.00	0.596	19.1	18.3	2.8	0.96	0.335	0.00795
3C172	285	285	23.3	0.70	2.53	299	299	14.6	0.74	4.00	0.0246
3C173.1	119.3	106.4	9.05	1.00	2.460	141.3	141.3	9.79	0.83	1.836	0.08472
3C175	159.9	159.9	9.77	0.58	2.47	232.3	214.4	10.8	0.44	3.42	0.1846
3C175.1	33.9	33.9	4.3	0.59	2.39	27.0	27.0	4.3	0.72	1.58	0.113
3C184	24.2	24.2	4.6	1.00	1.78	13.4	13.4	4.6	0.84	1.11	0.289
3C184.1	226.4	226.4	5.01	0.87	5.36	169	169	5.01	0.88	3.69	0.144
DA240	636.5	636.5	17.02	0.88	1.163	743.4	743.4	8.50	0.89	2.46	0.07744
3C192	126.8	126.8	3.17	0.83	5.23	107	107	2.3	0.98	3.43	0.0851
3C196	19.7	19.7	4.2	0.81	0.490	28.5	28.5	3.9	0.86	0.636	0.183
3C200	64.34	63.64	1.3	0.97	1.6	82.31	80.22	2.2	0.60	2.12	0.1226
4C14.27	117.1	117.1	6.74	0.99	3.64	80.35	80.35	6.47	1.00	1.514	0.1860
3C207	40.7	40.6	3.3	0.52	2.13	50.1	47.3	3.0	0.59	1.65	0.104
3C215	142.9	139.6	4.3	1.00	1.301	75.65	75.65	6.28	1.00	0.4254	0.3078
3C217	75.75	75.05	4.2	0.73	5.93	27.9	27.9	3.9	0.98	1.36	0.461
3C216	6.45	6.24	1.7	1.00	0.829	14.9	8.20	1.2	1.00	2.4	0.397
3C219	275.0	240.0	2.1	0.89	1.597	291.1	291.1	2.1	0.92	3.491	0.02848
3C220.1	98.49	98.49	10.1	0.79	1.77	117.9	117.4	8.89	0.71	1.556	0.08966
3C220.3	30.5	30.5	2.6	1.00	1.02	39.7	39.7	2.8	0.56	1.26	0.132
3C223	374.6	368.1	4.79	0.77	3.915	363.8	363.8	5.66	0.55	3.938	0.01461
3C225B	13.8	13.2	4.1	0.73	1.40	18.9	18.6	3.8	0.60	1.95	0.155
3C226	165.9	113.3	8.55	0.83	1.440	134.6	134.6	8.55	0.99	2.21	0.1041
4C73.08	661.1	516.2	23.86	0.80	1.371	470.3	386.1	44.64	1.00	0.9753	0.1687
3C228	163.6	163.6	11.9	0.76	3.89	143.8	136.4	11.9	0.92	2.156	0.06438
3C234	199.2	199.2	10.1	1.00	5.711	95.87	95.87	10.7	0.98	4.95	0.3501
3C236	1746	1746	87.66	0.78	2.932	2628	2151	111.4	0.64	7.880	0.2016
4C74.16	188.4	188.4	11.3	0.93	3.85	133.7	123.9	10.6	1.00	1.726	0.1699
3C244.1	152.0	152.0	7.16	0.75	5.00	137.3	134.3	6.10	0.91	5.27	0.05086
3C247	43.1	43.1	4.2	0.59	5.29	60.9	60.9	4.3	0.50	5.33	0.172
3C249.1	136.0	32.1	7.58	1.00	1.752	86.43	86.43	4.89	0.97	1.535	0.2229
3C254	92.66	92.66	3.0	0.33	–	33.3	16.6	3.1	1.00	1.33	0.472
3C263	226.5	226.5	8.81	0.49	5.78	114.5	114.5	12.2	1.00	1.518	0.3284
3C263.1	20.5	20.5	3.8	0.67	1.56	46.7	46.7	2.8	0.90	2.71	0.391

Table 14: Lobe properties

Source	North lobe					South lobe					χ_{lobe}
	LLS_{l} (kpc)	l (kpc)	RC (kpc)	f_{l}	R_{ax}	LLS_{l} (kpc)	l (kpc)	RC (kpc)	f_{l}	R_{ax}	
3C265	350.0	347.7	8.45	0.56	6.96	234.6	234.6	12.6	0.75	4.31	0.1974
3C268.1	188.0	188.0	12.9	0.54	8.59	151.0	151.0	10.1	0.44	4.22	0.1091
3C268.3	2.6	2.6	0.4	0.76	1.4	6.51	6.26	0.4	0.50	3.1	0.43
3C274.1	491.0	491.0	1.9	0.81	5.113	429.8	423.4	5.55	0.82	4.196	0.06652
3C275.1	78.46	75.42	1.4	1.00	8.11	43.0	43.0	2.1	0.71	1.76	0.292
3C277.2	315.2	300.3	7.84	0.56	5.90	123.6	123.6	12.0	0.85	2.15	0.4367
3C280	75.37	70.4	4.6	0.83	1.22	59.4	59.4	3.4	0.67	1.38	0.118
3C284	415.7	415.7	22.4	0.96	3.659	284.9	284.9	23.4	0.95	2.508	0.1867
3C285	120	110	7.72	1.00	1.3	145	145	8.25	0.96	1.1	0.094
3C289	43.5	43.5	4.2	0.73	2.41	40.9	40.9	4.6	0.70	2.18	0.0301
3C292	450.5	432.3	5.7	0.50	–	502.5	502.5	9.49	0.21	–	0.05459
3C295	13.6	13.6	1.2	0.96	1.13	19.7	19.7	1.2	0.74	1.23	0.186
3C299	15.3	14.9	3.1	0.80	1.80	44.5	44.5	2.8	0.36	–	0.487
3C300	284.5	284.5	19.5	1.00	4.562	117.3	109.5	26.9	1.00	1.203	0.4162
3C303	69.01	64.8	–	–	1.36	51.63	42.0	–	–	0.9881	0.1440
3C319	156.2	156.2	8.95	1.00	1.955	183.9	183.9	2.5	0.83	3.636	0.08156
3C321	264.3	264.3	–	–	–	266.8	259.5	–	0.15	–	0.004689
3C325	81.40	81.40	4.4	1.00	4.19	58.6	58.6	4.5	0.97	1.81	0.162
3C326	688.2	665.8	72.84	0.87	1.087	1253	1253	76.42	1.00	5.657	0.2910
3C330	195.8	195.8	26.3	0.55	3.52	202.7	202.7	23.6	0.77	3.39	0.01752
3C334	207.1	197.7	9.08	0.61	2.546	147.2	128.2	7.41	0.65	1.241	0.1690
3C336	119.2	119.2	13.0	1.00	3.20	82.17	82.17	8.80	1.00	1.33	0.1841
3C341	258	258	10.6	1.00	5.4	191	191	12.2	1.00	4.3	0.149
3C337	197.5	197.5	10.8	0.76	3.12	109.7	107.3	11.4	1.00	1.66	0.2860
3C340	174.0	170.7	10.8	0.82	3.10	153.1	153.1	12.0	0.80	2.44	0.06403
3C349	136.1	136.1	12.9	0.98	3.539	150.8	150.8	15.0	1.00	2.615	0.05125
3C351	138.8	129.7	24.1	1.00	0.7257	186.7	186.7	17.0	1.00	1.833	0.1471
3C352	53.7	49.8	4.1	0.66	1.36	47.3	46.5	4.2	0.89	1.93	0.0641
3C381	93.65	93.65	7.08	0.90	1.824	108.7	108.7	5.86	0.83	2.502	0.07434
3C382	99	99	0.78	1.00	2.4	100	96	0.43	0.46	1.7	0.018
3C388	47.2	37.4	–	–	2.31	38.1	34.7	–	–	1.47	0.107
3C390.3	142.4	142.4	3.65	0.85	3.658	101	101	4.14	0.70	1.33	0.170
3C401	36.90	36.27	1.7	1.00	1.57	42.86	42.86	2.0	0.85	1.82	0.07475
3C427.1	82.2	82.2	4.1	0.73	2.5	95.5	93.8	2.9	0.64	3.7	0.0747
3C433	75.8	44.8	0.47	0.5	5.4	60.7	60.7	0.47	1.0	2.40	0.111
3C436	201.4	201.4	9.58	0.99	2.262	173.2	166.6	9.58	1.00	2.131	0.07523
3C438	51.12	48.64	7.31	0.98	1.47	44.90	44.90	7.31	1.00	1.39	0.06479
3C441	78.39	72.72	6.5	1.00	1.22	183	183	7.90	0.75	3.22	0.400
3C452	208.8	199.4	4.88	1.00	2.385	218.8	217.5	3.58	0.99	2.559	0.02324
3C455	9.04	9.04	3.7	1.00	0.568	17.7	17.7	3.6	1.00	1.29	0.324
3C457	596.0	558.1	5.3	0.56	5.004	567.8	536.5	4.9	0.47	3.745	0.02428